Intra-grain orientation distributions in deformed aluminium: synchrotron X-ray diffraction experiment and crystal-plasticity finite-element simulation

Loïc Renversade, Romain Quey

Intra-grain orientation distributions in deformed aluminium: synchrotron X-ray diffraction experiment and crystal-plasticity finite-element simulation

Loïc Renversade[1] and Romain Quey[1]

[1] *Mines Saint-Etienne, Univ Lyon, CNRS, UMR 5307 LGF, F – 42023 Saint-Etienne, France*

Abstract

The development of intra-grain orientation distributions is analysed for 446 individual grains of an aluminium polycrystal deformed in tension to successive strains of 1, 1.5, 2, 2.5 and 4.5%. In the experiment, diffraction contrast tomography (DCT) and far-field 3D X-ray diffraction microscopy (3DXRD) were used, and a reduced-order representation of the intra-grain orientation distributions was determined from the broadening of the 3DXRD diffraction spots. A high-resolution finite-element simulation (700 elements/grain on average) was conducted on the same polycrystal, providing detailed information on orientation evolution. Several metrics were considered to analyse the experimental and simulated orientation distributions, including the average disorientation angles and the preferential disorientation axes. The average disorientation angles were found to increase almost linearly with strain, and to be in appreciable correlation between experiment and simulation (albeit evolving faster in simulation). It was shown that the preferential disorientation axes are distributed perpendicularly to the tensile direction (Z) and perpendicular to the X–Y component of the Rodrigues orientation vector. Detailed crystal plasticity analyses showed that the distribution of preferential disorientation axes is related to the presence of larger slip variabilities on particular slip systems. Using a simplified approach, it was shown that accurate knowledge of the average stress of a grain is necessary in order to predict the preferential disorientation axis, which is well-captured by the finite-element simulation. The intra-grain stress distribution appears to have comparatively less influence.

1 Introduction

The orientation distributions that develop inside grains of a polycrystal subjected to plastic deformation are important both for practical applications and for the basic understanding of the mechanisms from which they originate. In large-strain applications such as industrial rolling, intra-grain orientation distributions influence the mechanical properties [1] and subsequent annealing phenomena such as recrystallization nucleation [2, 3]. From the mechanics point of view, they hold archival information on the local deformation mechanisms, such as crystallographic slip or grain interaction, and the general development of heterogeneous stress and strain fields [4].

Historically, experimental (local) orientation distributions have been mostly observed in 2-D and after deformation, in single crystals or grains of polycrystals, primarily by electron backscattered diffraction (EBSD) and especially in the case of rolling-type deformation modes [5–7]. EBSD was also used in conjunction with the "microtexture tracking" or "split sample" technique, by which individual grains are followed on an internal surface of a sample, to access the orientation evolution with strain [8–10]. Experimental observations were compared to full-field simulations based e.g. on the crystal-plasticity finite-element method [11–13] to carry out detailed analyses of different attributes of the orientation distributions, which were considered in terms of distribution over all grains or correlated to microstructural attributes, in particular grain (average) orientation [4, 10, 14]. Actual grain-by-grain comparison between experiment and simulation on a general 3-D polycrystal potentially offers more information, but requires 3-D, non-destructive characterization of the microstructure before and during deformation. Such characterizations became possible with the advent of high-energy X-ray diffraction techniques, which have been applied mainly to uniaxial loadings [15]. This has lead to the so-called "far-field 3-D X-ray diffraction microscopy (3DXRD)" technique [16], which was first applied to follow the average rotations of grains in a plastically-deformed aluminium polycrystal [17] and compare them to predictions from simple models [18]. Derivative techniques were then developed to access intra-grain orientation information, such as diffraction-contrast tomography (DCT and 6D-DCT) [19, 20], which primarily facilitates mapping of undeformed or slightly deformed polycrystalline microstructures ($\varepsilon < 5\%$), or high-energy diffraction microscopy (HEDM) [21], which also applies to moderately deformed polycrystalline microstructures ($\varepsilon < 20\%$). Applications include Refs. [22,23]. However, the 3DXRD technique itself, which is experimentally simpler, also provides some degree of information on intra-grain orientation distributions [24]. Standard applications, which focus on the determination of the average orientations of grains, use only the average positions of the spots, but their broadening contains information on the orientation distributions (excluding the spatial arrangements), which can be used for example to determine the complete ODF of a deformed grain [25, 26], or directly compare experiment and simulation [27]. When the focus is specifically on the anisotropy properties of the orientation distributions, it should also be possible to determine them directly from the broadening of the diffraction spots.

In this work, an experiment based on DCT and 3DXRD is used to track the development, via the broadening of the diffraction spots, of the intra-grain orientation distributions in the grains of a deformed polycrystal subjected to tension, and the results are compared to those of a simulation based on the crystal-plasticity finite-element method. Using both data sets, the goal is to develop a better understanding of the development of the intra-grain orientation distributions. The paper proceeds as follows. First, the experiment and the method to determine the properties of the intra-grain orientation distributions from the observed diffraction spots are presented in Section 2. Then, the finite-element simulation and the procedure to determine the same properties are presented in Section 3. Next, the results on different metrics are presented and compared in Section 4. Section 5 relates the metrics, in particular the preferential disorientation axes, to deformation mechanisms, using a simplified approach. Section 6 completes the paper with conclusions.

2 Experiment

A high-purity Al–0.3wt% Mn alloy was used. After casting, the material was cold-rolled to 80% height reduction. A flat, dog-bone specimen was spark-machined with its tensile axis along the rolling direction, and with a gauge of section 1 mm × 1 mm and height 1.5 mm. The material was then recrystallized at 450 °C for 25 min. This resulted in a microstructure consisting of nearly equiaxed grains of an average size of about 150 µm with a relatively limited crystallographic texture. The grain orientations and reorientations developing as the specimen was subjected to plastic deformation were then observed *in situ* by high-energy X-ray diffraction at the Materials Science beamline of ESRF (ID11).

2.1 DCT and 3DXRD observation

Before deformation, the microstructure of the full gauge section of the specimen was mapped by DCT [28], see Figure 1a. This was done using a beam of energy 41.7 keV and a FReLoN camera with 2048 × 2048 pixels of an effective size of 1.4 µm, located 5 mm behind the sample. The X-ray beam was 1 mm wide and 550 µm high, so that three scans were necessary to cover a sample region of height 1.4 mm with an overlap of 75 µm between adjacent scans. Overlaps were used to facilitate the merging of the DCT polycrystal volumes corresponding to the different scans. The acquisition was done over a full sample revolution, with an integration step of 0.1° (3600 diffraction images) and an exposure time of 1 s. To merge the three volumes, registration was applied between their intersections, using the absorption homograms. Common grains between adjacent volumes were paired manually, and all pairs were finally merged automatically (this was done before the dilation step of the standard DCT post-processing). The average orientations of the grains subjected to merging were recomputed from the orientations of their pre-merging parts and did not change by more than 0.05°. The resulting polycrystal volume contained 1848 grains and is shown in Figure 1b and its texture in Figure 1c.

Deformation was then applied using the Nanox load frame [29], in several steps, to successive strains of 1, 1.5, 2, 2.5 and 4.5% (measured at the gauge section). After each deformation step, the grain orientations were measured by 3DXRD at the center of the gauge section, on a height of 550 µm [15]. This was done using a beam of energy 60 keV and a FReLoN camera with 2048 × 2048 pixels of an effective size of 48.5 µm, located 260 mm behind the sample. Up to the strain of 2%, a beam of height of 550 µm and width of 1 mm was used, and the acquisition was done over a full sample revolution, with an integration step of 0.03° (12,000 diffraction images) and an exposure time of 0.03 s. At higher strains, the acquisition parameters had to be adapted, due to the peak broadening resulting from plastic deformation, to avoid spot overlaps and excessive intensity loss. At a strain of 2.5%, the beam height was reduced to 275 µm, and two adjacent scans were acquired with an integration step of 0.06° (6000 diffraction images). At a strain of 4.5%, the height was reduced to 185 µm, and three adjacent scans were acquired with an integration step of 0.2° (1800 diffraction images) and an exposure time of 0.06 s. Standard post-processing was used to "index" the diffraction spots and relate them to the corresponding grains. The set of analysed grains is shown on Figure 1d, and typical orientation spots are provided in Figure 1e. Diffraction spots are inherently 3D intensity distributions, but are acquired as a set of 2D detector images (in $\boldsymbol{u}$–$\boldsymbol{v}$ directions) at fixed rotation angle (ω). For each spot, a stack of detector images can be used to reconstruct the full distribution. The distribution can then be projected into the azimuthal plane (η, ω) to retain only the lattice rotation information [15]. Only the spots that do not overlap with the spots of other grains were considered, which lead to sets of between 40 and 100 spots for each grain and at each strain. The resulting number of available spots tended to decrease as strain increased, but always remained higher than about 40 (which is sufficient to unambiguously and accurately determine the anisotropy properties of the corresponding orientation distribution). Among the total of 824 grains contained in the region covered by 3DXRD, 466 could be followed during the entire deformation and will be used in the following.

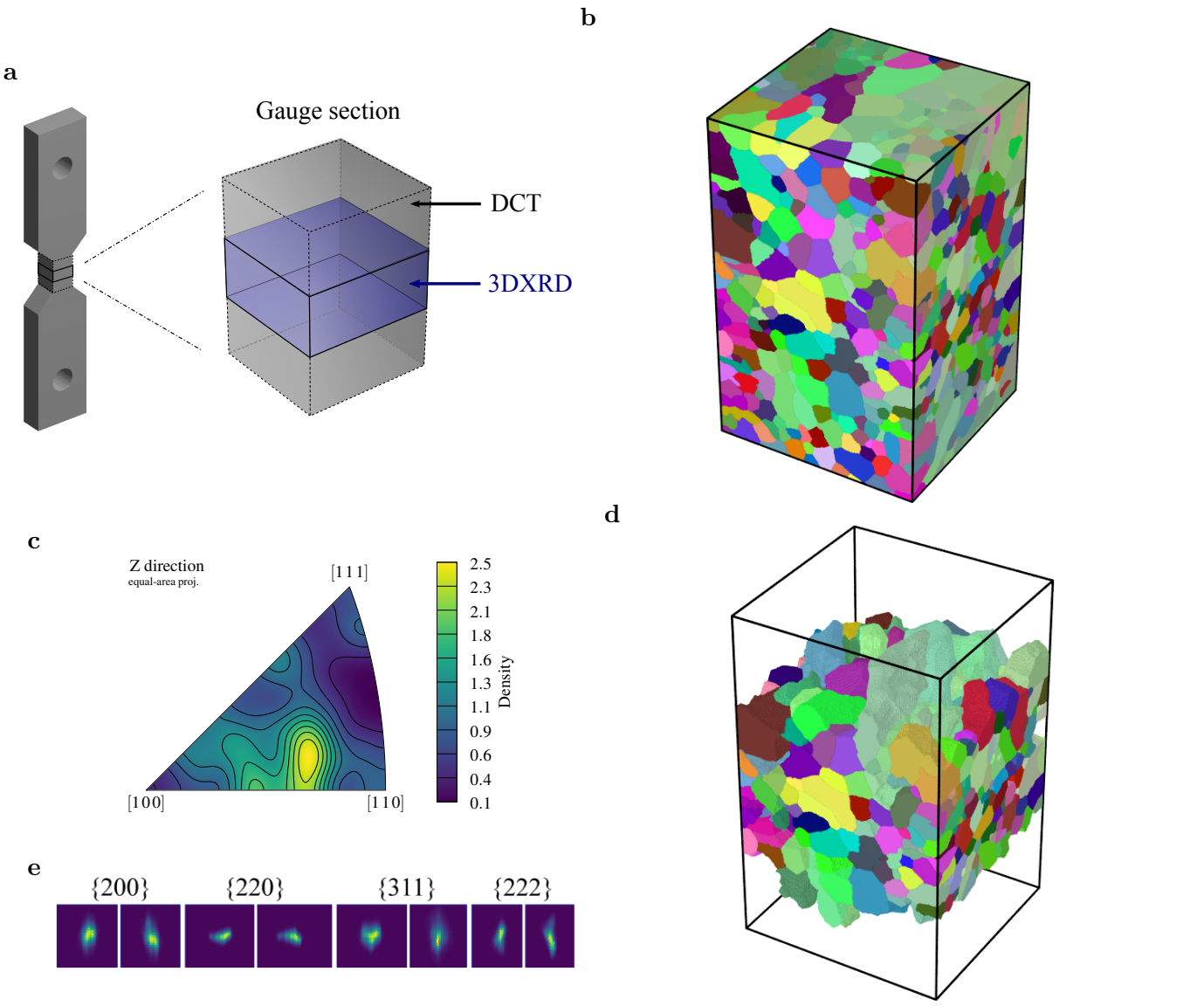

Figure 1: Principle and first results of the high-energy X-ray synchrotron experiment. (a) Tensile specimen and observed regions in DCT and 3DXRD, (b) initial microstructure obtained by DCT and colored by orientation, (c) crystallographic texture on the standard triangle (computed from the 466 followed grains), (d) grains followed by 3DXRD, and (e) example of a series of diffraction spots of a particular grain (azimuthal projection, $\varepsilon = 4.5\%$).

2.2 Determination of the intra-grain disorientation distributions

The orientation or disorientation distributions developing inside individual grains as a result of plastic deformation are typically unimodal and anisotropic, i.e. form a single "cloud" of orientations that extends differently depending on the direction [4,5], and it will also be the case in this work. In principle, multimodal orientation distributions can also develop, but only for grains of specific initial orientations and after large plastic strains [10,14]. For typical unimodal orientation distributions, the frequency profile along a direction of the orientation distribution is bell-shaped and approaches a normal distribution [4,6]. In this work, we are only interested in the (statistical) anisotropy properties of the orientation distributions and therefore will determine them directly from the diffraction spots, with no regards to the actual distributions. For each grain, the diffraction spots (described in azimuthal plane (η, ω)) correspond to intensity maps, I_{exp}, which constitute the input data to the approach.

2.2.1 Principle

For each grain, a reduced-order representation of the disorientation distribution is considered, and its parameters are determined from the set of intensity maps (I_{exp}). Formally, this corresponds to the process of fitting an analytical function to a collection of discrete data points, but with the analytical function and the discrete data points defined in different spaces.

The disorientation distribution of a grain is expressed in tangent space of orientation space, where the disorientation vector, $\boldsymbol{w}$, is defined as $\boldsymbol{w} = \boldsymbol{r}\,\theta/2$, where $\boldsymbol{r}$ and θ are the disorientation axis (expressed in the reference coordinate system) and disorientation angle, respectively [30]. The (anisotropic) disorientation distribution is defined as a 3-variate normal distribution, P,

$$P(\boldsymbol{w}) = \prod_{i=1}^{3} \frac{1}{\sqrt{2\,\pi\,{\theta_i}^2}} \exp\left(-\frac{(\boldsymbol{w}\cdot\boldsymbol{v_i})^2}{2\,{\theta_i}^2}\right), \tag{1}$$

where $\boldsymbol{v_i}$ are the three (orthogonal) principal directions of the distribution and θ_i are the associated characteristic lengths of the distribution ($\theta_1 \geq \theta_2 \geq \theta_3$). This function can be seen as the union of different rotation trends (θ_i) in three dominant (principal) directions ($\boldsymbol{v_i}$) that finally lead to the general, anisotropic distribution (P). By definition, P is centered on the origin of the space and integrates to 1 over the full space. The first principal axis ($\boldsymbol{v_1}$, associated to θ_1) corresponds to the disorientation axis about which the disorientation angles are the highest and will be referred to as "preferential disorientation axis" in the following [4].

The parameters of the disorientation distribution ($\boldsymbol{v_i}$ and θ_i) are determined using a method based on the generation of a set of diffraction spots, of intensities I_{gen}, from the disorientation distribution (often referred to as "forward simulation"[1]), and the optimization of its parameters so as to reproduce the set of experimental diffraction spots (I_{exp}) as closely as possible. First, initial $\boldsymbol{v_i}$ and θ_i values are considered: $\theta_{1,2,3}$ are set to $\delta\omega$ (the integration step of the 3DXRD scan), and $\boldsymbol{v_{1,2,3}}$ are simply set to be coincident to the axes of the reference coordinate system. Then, iterations are carried out on the values of $\boldsymbol{v_i}$ and θ_i (and so, on the disorientation distribution as a whole), until convergence, with these steps:

1. From $\boldsymbol{v_i}$ and θ_i, generate diffraction spots, I_{gen};
2. From the experimental and generated diffraction spots (I_{exp} and I_{gen}), compute their correspondence, r (correlation factor defined in the following);
3. From the evolution of r over iterations (i.e., as a function of $\boldsymbol{v_i}$ and θ_i), modify $\boldsymbol{v_i}$ and θ_i values so as to maximize r.

[1] In this article, the expressions "forward simulation" or "simulation" are not used to refer to the generation of diffraction spots to avoid confusion with the (finite-element) simulation.

Final results are values of $\boldsymbol{v_i}$ and θ_i, and therefore the disorientation distribution (P) corresponding to the set of intensity maps (I_{exp}) of a particular grain.

The generation of diffraction spots (item 1) is described in Section 2.2.2, while the spot comparison (item 2) is defined in Section 2.2.3 and optimization (item 3) is described in Section 2.2.4. An example of application is provided in Section 2.2.5.

2.2.2 Generation of diffraction spots from the reduced-order disorientation function

Given values of $\boldsymbol{v_i}$ and θ_i (which defines P), diffraction spots (to be compared to the experimental ones) are generated by first considering a "discrete approximation" of P, as illustrated on Figure 2. At small plastic strains, for which lattice rotations are limited, P is mostly contained within a small region about the origin of tangent space and its discrete approximation can appropriately be defined in this region. This region was taken as a cube of half edge length equal to $3\,\theta_1$ (the greatest "three standard deviations") to effectively contain most of the distribution, with N voxels along each direction. A value of $N = 80$ provided a good balance between the discretization accuracy and the computation time associated to the generation of the spots from the orientation distribution (which scales with N^3). The discrete approximation of P can then be processed as a set of weighted disorientations $\left\{(\boldsymbol{w^\alpha}, \phi^\alpha),\, \alpha = 1, ..., N^3\right\}$, where the disorientations ($\boldsymbol{w^\alpha}$) correspond to the centers of the voxels of the region, and the weights (ϕ^α) correspond to their P values ($\phi^\alpha = P(\boldsymbol{w^\alpha})$).

From the grain average orientation and the discretized disorientation distribution ($\{\boldsymbol{w^\alpha}, \phi^\alpha\}$), a set of orientations, $\{(\boldsymbol{q^\alpha}, \phi^\alpha)\}$, was generated, and the diffraction spots corresponding to their ($h\,k\,l$) reflections were then computed using the standard forward projection relation [15]. For each weighted orientation of the distribution, ($\boldsymbol{q^\alpha}$, ϕ^α), a weighted diffraction vector, $((\eta^\alpha, \omega^\alpha), \phi^\alpha)$, was obtained, and its weight (ϕ^α) was added to the intensity of the corresponding bin of the (η, ω) grid. Considering the contribution of all orientations, an intensity map, I^0_{gen}, is generated. However, as it is generated only from the discrete approximation of the disorientation distribution, it does not include the effects of other microstructural or experimental factors that affect the experimental intensity map). These effects must be taken into account to lead an unbiased comparison of the experimental and generated intensity maps (I_{exp} and I_{gen}). A possibility would be to decorrelate the experimental intensity maps from these effects, but the effects can equivalently be "added" to the generated intensity maps. The first operation is related to the ODF discretization and the integration of the intensities of the diffraction vectors (which is done independently of the distance to the bin center or the distance to the centers of the neighboring bins) and introduces "smoothing", similar to an experimental "broadening effect" of the detector itself, and the second operation introduces a "grain size effect", which causes broadening along η. The actual generated intensity map, I_{gen}, was therefore obtained as

$$I_{\text{gen}}(\eta,\, \omega) = I^0_{\text{gen}}(\eta,\, \omega) \circ G_1(\eta,\, \omega) \circ G_2(\eta), \tag{2}$$

where $\circ$ is the convolution product. The ODF discretization correction, $G_1(\eta,\, \omega)$, is defined as

$$G_1(\eta,\, \omega) = \frac{1}{\sqrt{2\,\pi\,\delta r^2}}\, \exp\left(-\frac{\eta^2\, +\, \omega^2}{2\,\delta r^2}\right), \tag{3}$$

where δr is the bin size of the (η, ω) grid. The grain size effect, $G_2(\eta)$, is defined as

$$G_2(\eta)\; =\; \frac{1}{\sqrt{2\,\pi\,{r_i}^2}}\, \exp\left(-\frac{\eta^2}{2\,{r_i}^2}\right), \tag{4}$$

where r_i is the grain equivalent radius (determined by DCT or, equivalently, by 3DXRD, using the average spot intensity of the grain [31]) expressed in units of η. An example of generated diffraction spot is provided in Figure 2c.

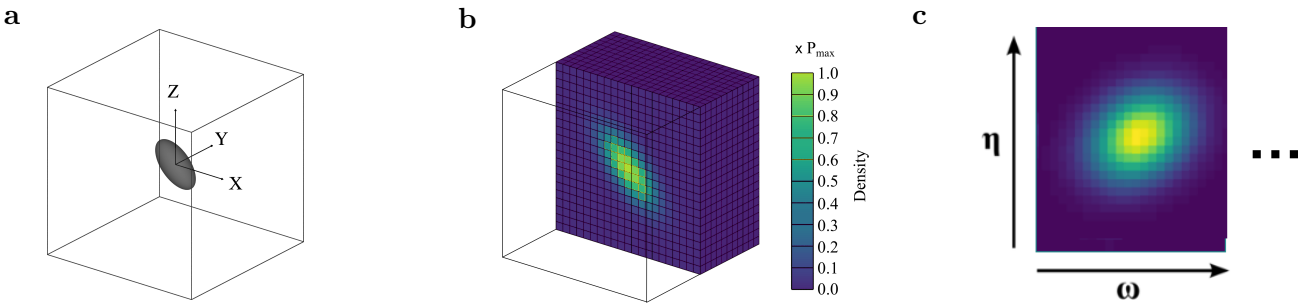

Figure 2: Discretization of a grain ODF. The parameter values are $\lambda_1 = 0.0087$ ($\simeq 1°$) and $\lambda_2 = \lambda_3 = 0.0044$ ($\simeq 0.5°$). $\Delta r = 0.0524$ ($\simeq 6°$) and $N = 23$, resulting in $\delta r = 0.0022$ ($\simeq 0.25°$). (a) Disorientation distribution represented as an ellipsoid showing the isosurface at one standard deviation in the discretization domain. (b) Discretized disorientation distribution in a domain containing 12167 voxels (in practice, $N^3 = 512,000$ voxels are used). (c) Corresponding intensity map in the (η, ω) plane (I_{gen}).

2.2.3 Correspondence between experimental and generated diffraction spots

The correspondence between an experimental spot and a generated spot is quantified by the Pearson product-moment correlation coefficient, r, which is defined as

$$r = \frac{\sum_{i,j} \left(I^{ij}_{\text{exp}} - I_{\text{exp}}\right)\left(I^{ij}_{\text{gen}} - I_{\text{gen}}\right)}{\sqrt{\sum_{i,j} \left(I^{ij}_{\text{exp}} - I_{\text{exp}}\right)^2} \sqrt{\sum_{i,j} \left(I^{ij}_{\text{gen}} - I_{\text{gen}}\right)^2}}, \tag{5}$$

where (i, j) loops over all bins, $I_\bullet$ is the average of $I^{ij}_\bullet$ over all bins, and r reaches the maximal value of 1 for a perfect linear correlation. The correlation coefficient (r) is insensitive to the difference in average values, so that the generated spots do not have to be defined by actual intensities. The objective function (to maximize) is then simply expressed as

$$r = \frac{1}{N} \sum_{k=1}^{N} r_k, \tag{6}$$

where N is the number of diffraction spots.

2.2.4 Optimization

While the set of principal axes ($\boldsymbol{v_i}$) and characteristic length (θ_i) represent a total of 12 variables, the principal axes ($\boldsymbol{v_i}$) form a coordinate system whose orientation with respect to the reference coordinate system can be described by a (3D) Rodrigues vector, thereby reducing the total number of variables from 12 to six. Determining the values of the six variables so as to maximize r consists of a non-linear optimization problem, of unknown gradient, which is solved using the local optimization algorithm Subplex of the NLopt library [32, 33]. The Subplex algorithm is derived from the Nelder-Mead simplex algorithm and decomposes high-dimensional problems into a series of low-dimensional problems that can be handled by the simplex algorithm.

2.2.5 Example of grain 1212

The method is applied to a particular grain (grain 1212), of an average size of 60 µm and an arbitrary orientation (26° away from Cube). For this grain, 91 spots at $\varepsilon = 1\%$ down to 47 spots at $\varepsilon = 4.5\%$ were obtained from the experimental data. The evolution of eight spots that were available at all deformations is showcased in Figure 3a, and some of their anisotropy properties and r value are provided in Table 1. It can be

clearly seen that, as deformation accumulates, the experimental diffraction spots broaden and show different elongated shapes depending on the $(h\,k\,l)$ direction, but also depending on the strain, which indicates that the anisotropy properties of the orientation distribution evolve during deformation. The generated spots properly capture the size, shape and direction of the experimental spots at all strains. Clearly, they also "simplify" the experimental spots, which are less regular and sometimes exhibit local fluctuations, but the differences can be considered of second order relative to the global, anisotropic character of the distribution. Some degree of fluctuation, in particular, may be associated to experimental noise, which the reduced-order representation allows to "filter". For the grain of interest, the correlation coefficient (r) increases with strain to a value as high as 0.95 at $\varepsilon = 4.5\%$, which tends to confirm that 3-variate normal distributions can be used to represent the orientation distributions of grains deformed to a plastic strain of a few percents [6].

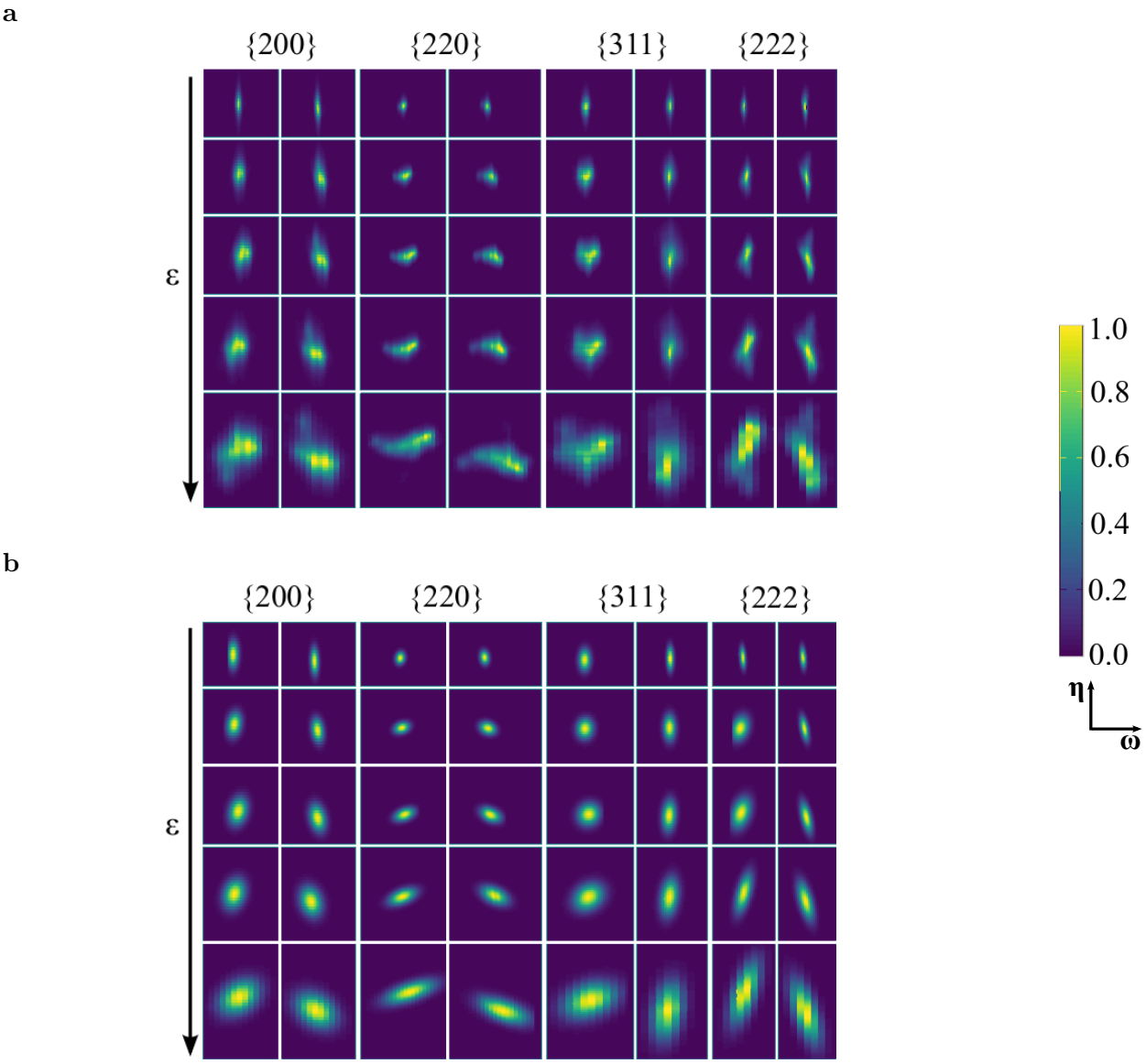

Figure 3: Comparison between experimental and generated spots for an arbitrary grain (grain 1212): (a) experimental and (b) generated. The spots are arranged by types of reflection (horizontally) and strain levels (vertically), and are normalized to a maximal intensity of 1. The $(h\,k\,l)$ directions are $(2\,0\,0)$, $(\bar{2}\,0\,0)$, $(2\,2\,0)$, $(2\,\bar{2}\,0)$, $(3\,1\,\bar{1})$, $(\bar{1}\,\bar{3}\,\bar{1})$, $(2\,\bar{2}\,2)$ and $(\bar{2}\,2\,\bar{2})$, from left to right, and the successive strains are $\varepsilon = 1$, 1.5, 2, 2.5 and 4.5%.

Table 1: Assessment of intra-grain orientation distributions: results of the optimization approach for an arbitrary grain (grain 1212). $\boldsymbol{v_1}$ is expressed in the reference coordinate system.

Strain	Number of spots	θ_1 (°)	θ_2 (°)	θ_3 (°)	$\boldsymbol{v_1}$	r
1.0%	91	0.08	0.04	0.02	(0.836, 0.119, −0.536)	0.80
1.5%	83	0.16	0.08	0.05	(0.936, 0.194, −0.292)	0.86
2.0%	78	0.22	0.09	0.07	(0.946, 0.147, −0.288)	0.88
2.5%	44	0.30	0.13	0.09	(0.963, 0.050, −0.266)	0.93
4.5%	47	0.56	0.25	0.15	(0.962, 0.060, −0.267)	0.95

3 Simulation

The plastic deformation of the polycrystal was simulated over the region mapped by DCT in order to predict the resulting lattice reorientations of the grains, and the 466 grains followed by 3DXRD were used for the analysis. Having a simulation region (the DCT region) significantly larger than the analysis region (the 3DXRD region) made it possible to consider the real neighbors of the grains of the analysis region and to apply the boundary conditions sufficiently far from these grains not to affect their reorientations. The polycrystal deformation was simulated using the crystal-plasticity finite-element method, in which the grains of the polycrystal are discretized into finite elements, deform by slip on specific crystallographic systems, and interact according to mechanical equilibrium to develop heterogeneous stress and strain fields. The free / open-source software packages Neper and FEPX were used for the polycrystal meshing, parallel simulation deformation and result post-processing [13, 34, 35].

3.1 Constitutive equations

Plastic deformation occurs by slip on the 12 $\{1\,1\,1\}\langle 1\,1\,0\rangle$ systems. The slip rate of a given slip system, $\dot{\gamma}^\alpha$, is related to its resolved shear stress, τ^α, through a power law,

$$\dot{\gamma}^\alpha = \dot{\gamma}_0 \left| \frac{\tau^\alpha}{g^\alpha} \right|^{\frac{1}{m}} \operatorname{sgn}\left(\tau^\alpha\right), \tag{7}$$

where $\operatorname{sgn}(x) = 1$ if $x \geq 0$ and $\operatorname{sgn}(x) = -1$ if $x < 0$, m is the strain-rate sensitivity coefficient, $\dot{\gamma}_0$ is the fixed-state strain rate scaling coefficient, and g^α is the current system strength. The hardening on a slip system, $\dot{g}^\alpha$, is described by a Voce hardening assumption,

$$\dot{g}^\alpha = h_0 \left(\frac{g_s - g^\alpha}{g_s - g_0} \right)^n \dot{\gamma}, \qquad \text{where } \dot{\gamma} = \sum_\alpha |\dot{\gamma}^\alpha|. \tag{8}$$

At the initial state ($\varepsilon = 0$), all g^α are taken equal to the g_0 value. In such a case, it can be noticed from Eq. 8 that the yield surface grows isotropically with strain. The material parameters were identified from the experimental stress-strain behavior, and their values are $\dot{\gamma}_0 = 1\ \mathrm{s}^{-1}$ (a convention), $m = 0.03$, $h_0 = 47$ MPa, $g_0 = 6$ MPa, $g_s = 455$ MPa and $n = 2.6$. The crystal elastic anisotropy was modelled using stiffness parameters of $C_{11} = 107.3$ GPa, $C_{12} = 60.9$ GPa and $C_{44} = 56.6$ GPa [36]. A complete description of the constitutive model and the finite element method implementation can be found in Refs. [11, 12].

3.2 Polycrystal meshing and deformation

The polycrystal image obtained by DCT was defined in raster format, using voxels. In contrast, the synthetic polycrystals typically used in finite-element crystal-plasticity simulations are defined in vector format, using points, straight edges, planar faces and (convex) volumes, which is the input of standard meshing tools [34, 37]. In this work, such a description was accordingly obtained by approximating the polycrystal image by its nearest convex-grain geometry, using the general approach presented in Ref. [35]. Formally, any polycrystal made of convex grains which meet along grain boundaries, triple lines and quadruple points, such as the polycrystal used in this work but also most single-phase (and some multi-phase) polycrystals, corresponds to a normal tessellation, and any normal tessellation can be represented by a Laguerre tessellation [38]. It is therefore possible to approximate a polycrystal by an optimal convex-cell geometry using a Laguerre tessellation, given proper determination of its parameters.

Given a spatial domain $D \in \Re^n$, a Laguerre tessellation is defined from a set of seeds, S_i, described by their positions, $\boldsymbol{x_i}$, and weights, w_i, where each seed (S_i) generates a Laguerre cell, C_i, as follows:

$$C_i = \left\{ P(\boldsymbol{x}) \in D \mid d(\boldsymbol{x}, \boldsymbol{x_i})^2 - w_i < d(\boldsymbol{x}, \boldsymbol{x_j})^2 - w_j \ \ \forall j \neq i \right\}, \tag{9}$$

where d is the Euclidean distance. In 3D, and under the Laguerre tessellation parameterization, any normal tessellation comprising N cells (and so any polycrystal made of N convex grains) can therefore be described by a set of a maximum of $4\,N$ parameters. It is, however, non trivial to determine the values of these parameters. In this work, this was done by minimizing an objective function, O, that quantifies the difference between the input (DCT) polycrystal and the output (convex-cell) tessellation in terms of distance between their internal boundaries [35],

$$O = \sqrt{\frac{2}{n_v \langle d \rangle^2} \sum_{i=1}^{N} \sum_{v_k \in G_i^b} d\left(v_k,\, C_i\right)^2} \quad \text{with} \quad n_v = \sum_{i=1}^{N} |G_i^b|, \tag{10}$$

where G_i^b represents the set of boundary voxels of grain i, $d\left(v_k,\, C_i\right)$ is the Euclidean distance between a boundary voxel of grain i, $v_k \in G_i^b$, and its corresponding cell, C_i, $\left|G_i^b\right|$ is the number of elements of G_i^b, n_v is the total number of boundary voxels, and $\langle d \rangle$ is the average grain size [35].[2] The optimization problem is large-scale, non-linear and of unknown gradient, and was solved using the local optimization algorithm subplex of the NLopt library [32, 33, 35]. The final average distance between the grain boundaries of the polycrystal and those of the approximating tessellation was 10 µm.

The cells were then assigned the crystal orientations of the grains, and the tessellation was regularized so as to remove its smallest edges and faces, which avoids the generation of low-quality elements during meshing [34]. The tessellation was finely and homogeneously discretized into 10-node tetrahedral elements, with an average of 700 elements per grain, which lead to a mesh comprising about 1,338,000 elements and 1,833,000 nodes, as shown in Figure 4a.

The mesh was subjected to the experimental deformation of 4.5% tension (at a strain rate of 10^{-2} s^{-1}) by imposing a non-zero z velocity to the top surface while the bottom surface remained fixed along z (with additional constraints to avoid rigid body motions). Figure 4b provides an example of results on the deformed mesh.

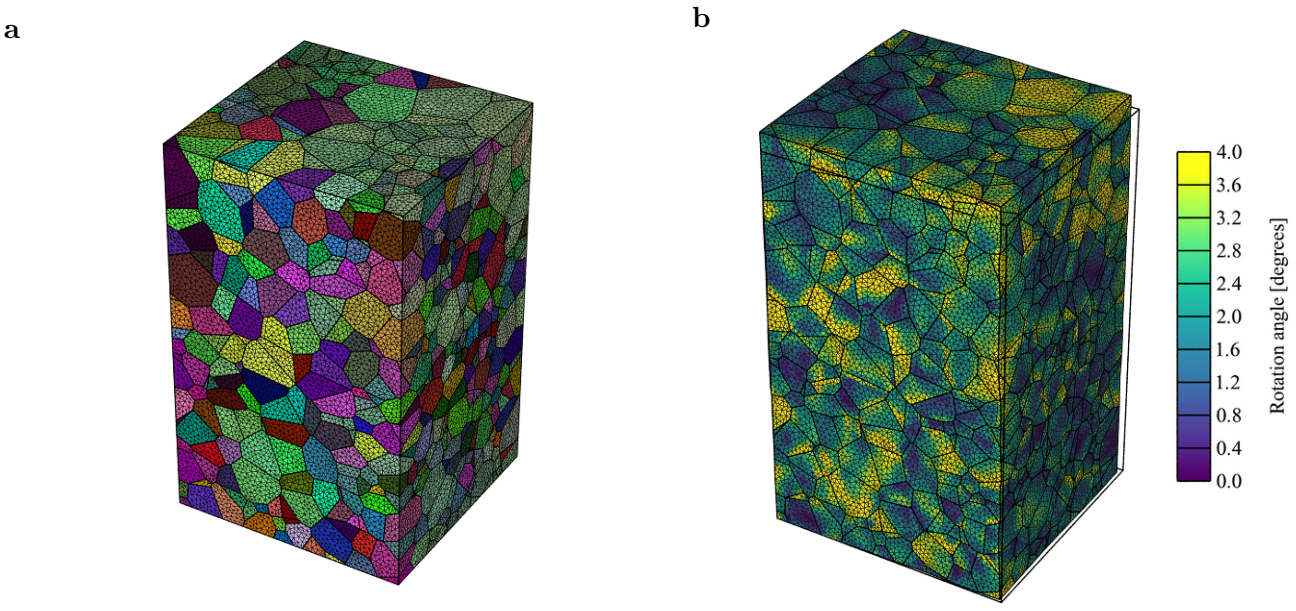

Figure 4: Principle and first results of the finite-element simulation. (a) mesh, and (b) lattice rotation angle (from the initial orientation) at 4.5%.

[2] The expression differs from the one used in Ref. [35] by a scaling factor, but this does not affect the optimization nor final tessellation.

3.3 *Determination of the intra-grain disorientation distributions*

For each grain (and at each strain), the finite-element simulation provides a set of weighted orientations (corresponding to the elemental orientations and volumes), $\{(\boldsymbol{q}^{\boldsymbol{\alpha}}, \phi^{\alpha}), \alpha = 1, \ldots, N\}$, from which the anisotropy parameters $\boldsymbol{v_i}$ and θ_i of the disorientation distribution can be determined. The average grain orientation, $\overline{\boldsymbol{q}}$, is first computed by quaternion averaging [4,5]. For each element of the grain, the disorientation with respect to the average orientation is then computed and written as the disorientation vector, $\boldsymbol{w}^{\boldsymbol{\alpha}}$ (associated to its weight, ϕ^{α}).

The anisotropy parameters of the discrete disorientation distribution can then be computed directly (i.e., without actually fitting the distribution[3]), as first proposed by Glez and Driver [5] for EBSD data and Barton and Dawson [39] for crystal-plasticity finite-element data, as illustrated on Figure 5. Given the set of weighted disorientations expressed in tangent space, $\{(\boldsymbol{w}^{\boldsymbol{\alpha}}, \phi^{\alpha}), \alpha = 1, \ldots, N\}$, a 3×3 covariant matrix, $\boldsymbol{S}$, is defined as

$$\boldsymbol{S} = \frac{1}{\Phi} \sum_{\alpha=1}^{N} \phi^{\alpha} (\boldsymbol{w}^{\boldsymbol{\alpha}} \otimes \boldsymbol{w}^{\boldsymbol{\alpha}}) \quad \text{with} \quad \Phi = \sum_{\alpha=1}^{N} \phi^{\alpha}, \tag{11}$$

which is symmetric and can be diagonalized. The eigenvectors and the square roots of the eigenvalues of $\boldsymbol{S}$ can be identified to the principal directions and characteristic lengths of the disorientation distribution P (Equation 1), $\boldsymbol{v_i}$ ($i \in \{1, 2, 3\}$) and θ_i, respectively.

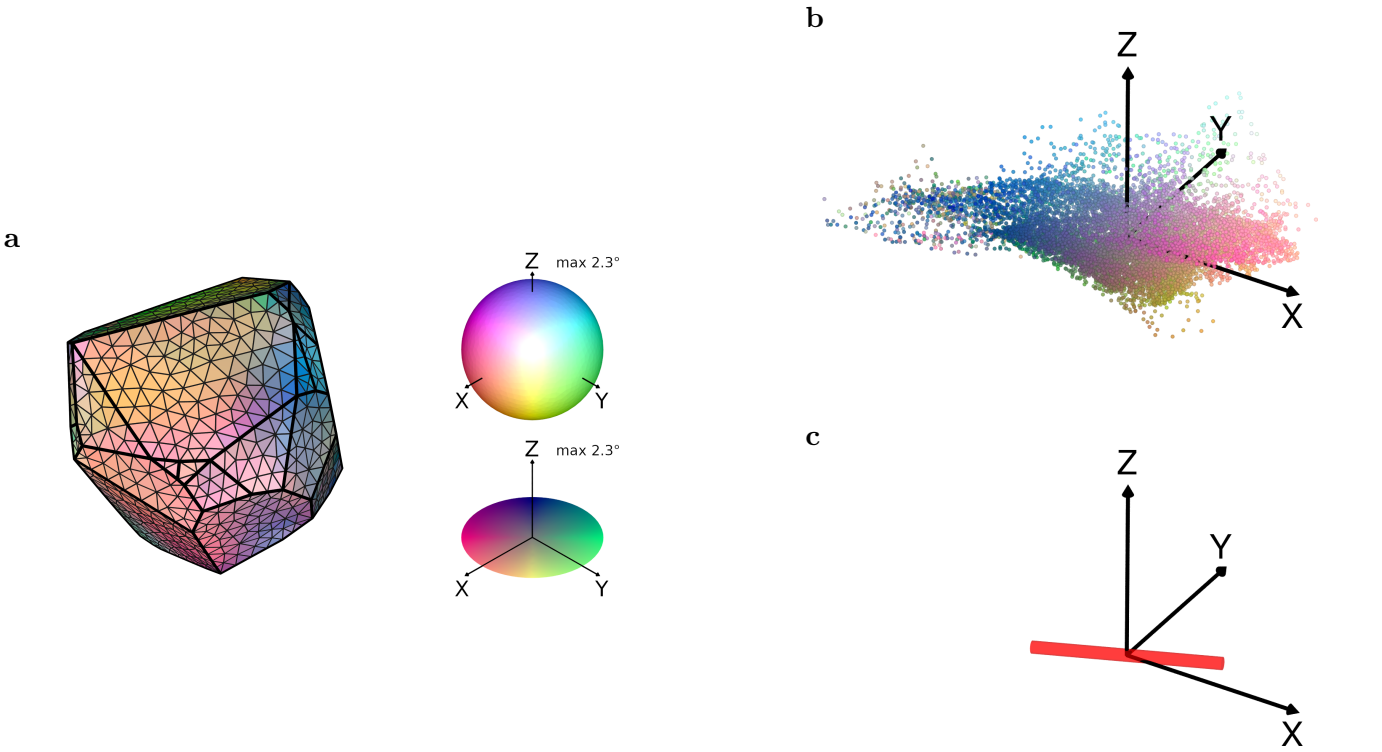

Figure 5: Illustration of the computation of the preferential disorientation axis from discrete orientation sets. Example of grain 1212 at $\varepsilon = 4.5\%$. (a) Disorientations ($\boldsymbol{w}^{\boldsymbol{\alpha}}$) represented on the mesh of the grain. The color key is defined in tangent space, as a ball of radius corresponding to a maximal disorientation of 2.3°. (b) Disorientations ($\boldsymbol{w}^{\boldsymbol{\alpha}}$) represented in tangent space, using the same colors as in (a). (c) Preferential disorientation axis ($\boldsymbol{v_1}$) computed from Equation 11.

[3] Fitting a 3-variate normal distribution to the discrete disorientation set of the grain, similar to the experimental approach, would be another possibility, but would lead to very close results for significantly larger complexity.

4 Results

Attributes of the intra-grain orientation distributions were analysed for the 466 tracked grains, in experiment and simulation. In the following, we first define some metrics to describe the orientation distributions and analyse trends in these metrics using distributions. We then look for grain-by-grain correlations between experiment and simulation, and correlations with the average grain orientation.

In the cases of results computed over all grains (average values, distributions, etc.), and due to the presence of (non-random) texture in the set of investigated grains (see Figure 1d), a texture correction is applied so as to obtain results that are representative of a texture-free material (in place of the polycrystal specifically considered). The texture correction defines a weight for each grain, from the size of the "local neighborhood" of its orientation (on the IPF, which is the appropriate space under the uniaxial symmetry condition). It follows that clustered orientations, which tend to over-represent particular orientations, have smaller weights, while isolated orientations, which represent large portion of possible orientations, have larger weights. The method is described in Section A, and the obtained (relative) grain weights vary from 0.07 to 8.

4.1 Average disorientation angle and anisotropy factor

The angular extent of the orientation distribution of a grain is typically quantified as the average disorientation angle with respect to the average orientation, $\bar{\theta}$ [4, 10], and is straightforward to compute in the case of discrete orientation sets (simulation results). In the case where only the anisotropy parameters of the orientation distribution (θ_i, $\boldsymbol{v_i}$) are known (experimental results), it can be computed with high accuracy as

$$\bar{\theta} = a\ (\theta_1{}^p + \theta_2{}^p + \theta_3{}^p)^{\frac{1}{p}}\,, \tag{12}$$

with $a = \sqrt{2/\pi}$ and $p = 1.58$ (see Appendix B). The distributions of the average disorientation angles at successive strains are provided in Figure 6, and the corresponding average values are provided in Table 3, for experiment and simulation. In both cases, the average disorientation angles increase gradually with strain. On average over all grains, the average disorientation angle increases almost linearly with strain, at rates of 0.08 and 0.18° per percent strain, for experiment and simulation, respectively. The constant rate of evolution can be explained by the fact that the deformation remains small enough so that the average orientation does not change significantly and the deformation conditions (slip rates, etc.) and therefore the reorientation conditions (including the disorientation distribution evolution) remain nearly the same [4]. The faster evolution in simulation was not observed in a previous work on the same material (deformed in hot plane strain compression to large strains) [4], but may be related to a smaller strain-rate sensitivity (m, see Equation 7), as using a larger value indeed reduces the θ_m values.

The strength of the anisotropy of the orientation distribution of a grain can be described by an "anisotropy factor", θ_a, defined as

$$\theta_a = \theta_1 / \sqrt[3]{\theta_1\,\theta_2\,\theta_3}, \tag{13}$$

which takes a minimal value of 1 for an isotropic distribution. θ_a just serves for the comparison between experiment and simulation; specifically, it is not particularly related to any physical phenomenon, and other applications actually suggested expressions based on additive rather than multiplicative composition [3]. The distribution of the anisotropy factors are provided in Figure 7 for experiment and simulation, and the corresponding average values are provided in Table 3. Experiment and simulation show comparable distributions and average values of 1.7–2.0, while only the experimental anisotropy factors tend to increase with strain.

The experimental and simulated average disorientation angles and anisotropy factors at all strains are compared grain-by-grain in Figure 8. The θ_m values show appreciable correlation, with a linear correlation coefficient higher than 0.45 for strains of 1.5% and larger, while the anisotropy factors show only low correlation, if any.

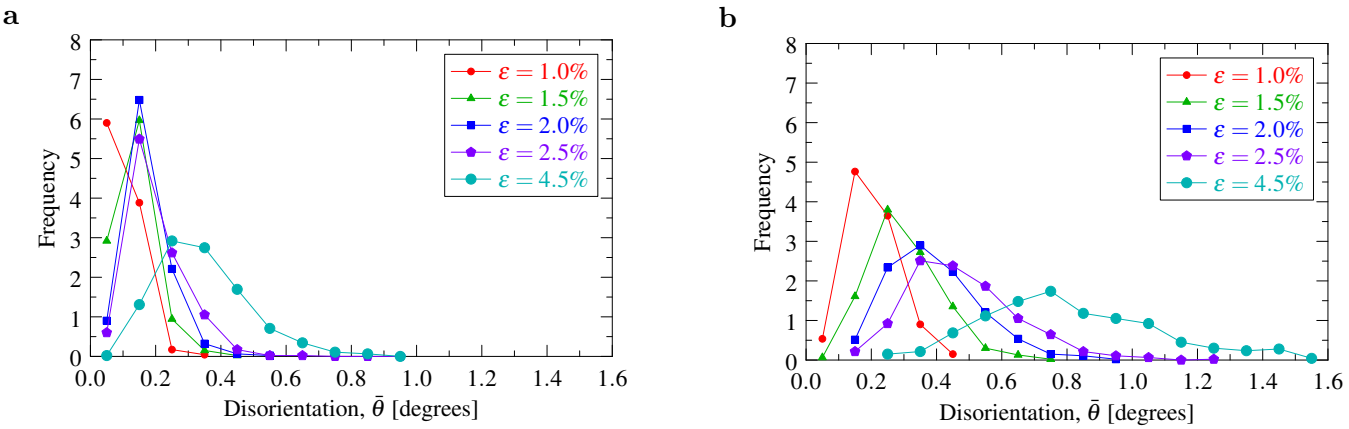

Figure 6: Distributions over all grains of the average disorientations, $\bar{\theta}$. (a) experiment and (b) simulation.

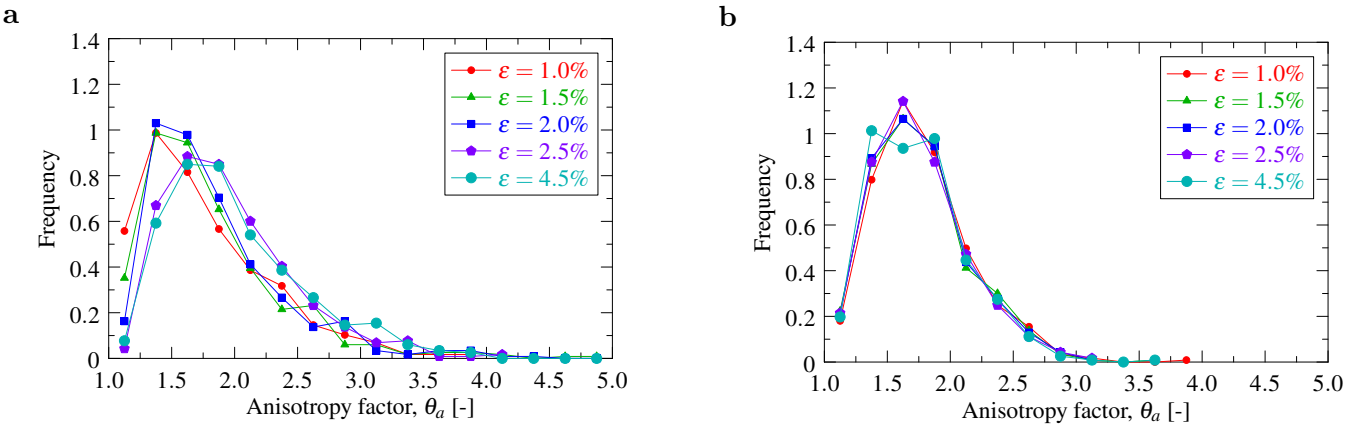

Figure 7: Distributions over all grains of the anisotropy factors, θ_a. (a) experiment and (b) simulation.

Strain	Average disorientation angle, $\overline{\theta}$ [°]		Average anisotropy factor, θ_a [-]	
	Experiment	Simulation	Experiment	Simulation
1.0%	0.10	0.20	1.75	1.78
1.5%	0.14	0.30	1.81	1.77
2.0%	0.17	0.39	1.85	1.76
2.5%	0.20	0.48	1.96	1.76
4.5%	0.35	0.82	2.03	1.75

Table 2: Evolution of the average disorientation angles and anisotropy factors with strain in the experiment and simulation.

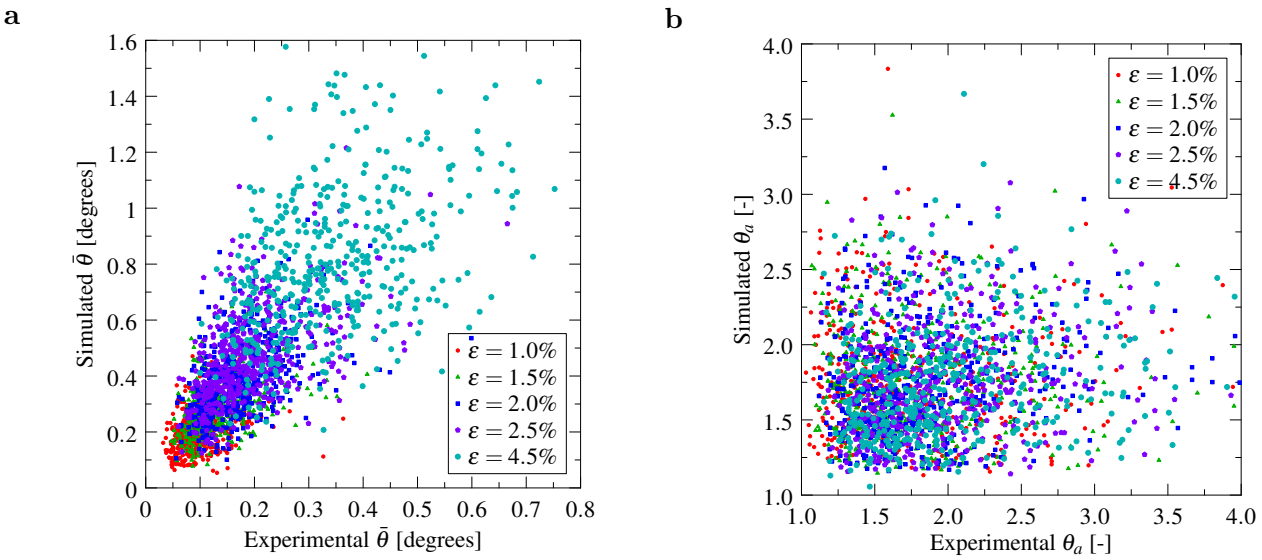

Figure 8: Grain-by-grain comparison between experiment and simulation of (a) the average disorientation angle ($\bar{\theta}$) and (b) the anisotropy factor (θ_a). Note the different x and y scales in (a).

Strain	Linear correlation coefficient [-]	
	Average disorientation angle, $\overline{\theta}$	Anisotropy factor, θ_a
1.0%	0.32	$\simeq 0$
1.5%	0.47	$\simeq 0$
2.0%	0.47	0.16
2.5%	0.48	0.17
4.5%	0.45	0.18

Table 3: Correlation between the grain average disorientation angles and anisotropy factors in experiment and simulation.

4.2 Preferential disorientation axis

The distributions of preferential disorientation axes ($\boldsymbol{v_1}$) at successive strains are provided in Figure 9, for both experiment and simulation. The equal-area projections are plotted onto the sample X–Y plane (Z = tensile direction), with uniaxial symmetry applied to the density field. Figure 9 shows that, in the experiment, the axes are initially almost uniformly distributed and then become perpendicular to the tensile direction as strain increases. A smooth transition occurs with strain, and the distribution becomes clearly defined from a strain of 2%. In the simulation, the distributions are very similar at all strains and show the same distribution of axes perpendicular to the tensile direction. The simulated distribution is slightly more diffuse than the two final experimental ones (strains of 2.5 and 4%).

Figure 10 provides the distributions of the angles between the experimental and simulated preferential disorientation axes ($\boldsymbol{v_1}^{\text{exp}}$ and $\boldsymbol{v_1}^{\text{sim}}$, respectively) at successive strains. The distributions show that the agreement between experiment and simulation improves as strain increases, which is consistent with the progressive evolution of the experimental distributions toward the simulated distributions (distributions perpendicular to the tensile direction). A possible interpretation for an agreement improving with strain is that, at larger strains, and in particular after the elastic-plastic transition [36], the stress state "stabilizes" in a specific vertex of the yield surface, and that this occurs more rapidly in the simulation than in the experiment.

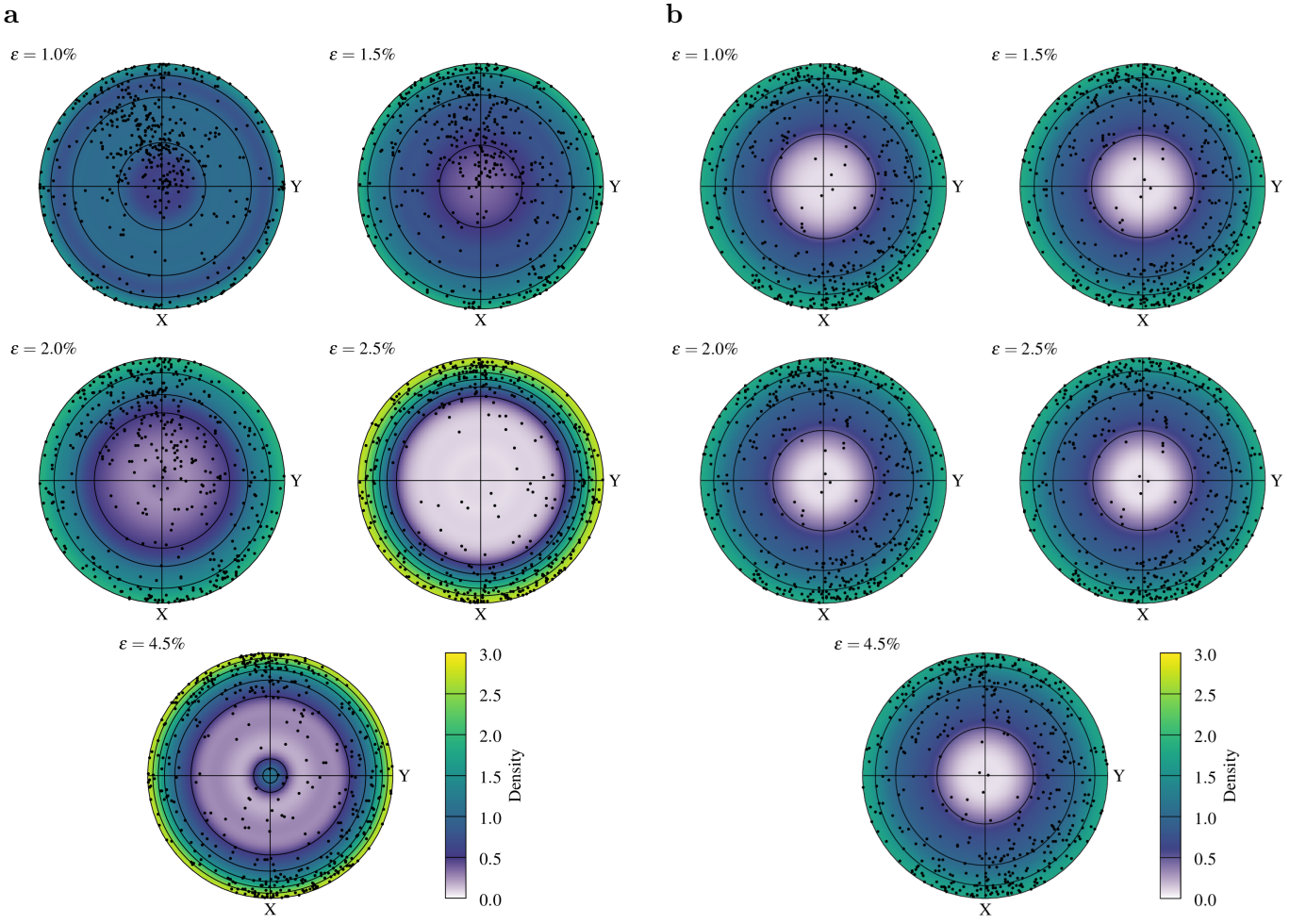

Figure 9: Distributions over all grains of the preferential disorientation axes, $\boldsymbol{v_1}$, at increasing strains, in (a) experiment and (b) simulation. On the (equal-area) projections, the tensile axis (Z) is at the center of the figures, the data of each grain is represent by a dot, and uniaxial symmetry is applied to compute the density field (data averaging at constant distance from the origin).

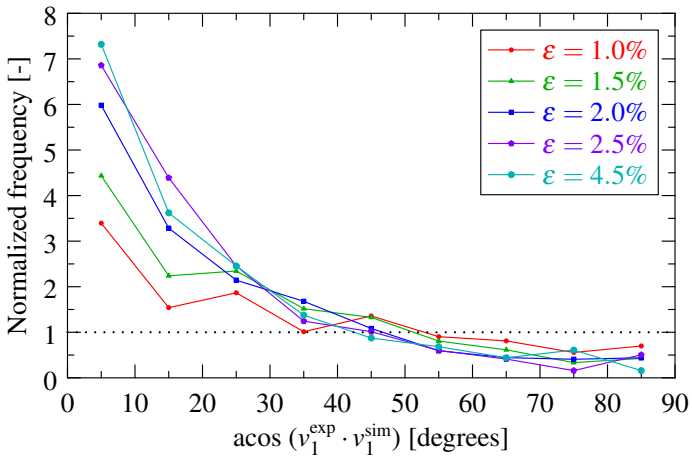

Figure 10: Distribution of the correlations between the experimental and simulated preferential disorientation axes ($\boldsymbol{v_1}^{\text{exp}}$ and $\boldsymbol{v_1}^{\text{sim}}$, respectively). The frequency plots are normalized with respect to the case of a random direction distribution (dotted line).

4.3 Correlation of the preferential disorientation axis with grain average orientation

To investigate the relationships between the preferential disorientation axes and the corresponding average orientations of the grains, the preferential axes can be plotted in the fundamental region of the Rodrigues orientation space [40]. The locations of the typical orientation fibers (Z ∥ ⟨1 0 0⟩, ⟨1 1 0⟩ and ⟨1 1 1⟩) are shown in Figure 11. The distributions of the preferential axes in the fundamental region, at successive strains and both for experiment and simulation, are plotted in Figures 12 and 13, as 3D views and views along the tensile direction (Z), respectively. The views along Z somehow allow to "reduce" the data set according to the uniaxial symmetry conditions. In Figure 12, the apparent non-uniform distribution of batons in Rodrigues space is due to the combined effects of the (non-random) texture and a higher density of Rodrigues space at the origin. A preferential disorientation axis is represented as a small baton as follows [4]:

- The radius and length are constant.
- The barycenter is on the average orientation.
- The axis is along the preferential disorientation axis, in orientation space.
- The color is related to the preferential disorientation axis components. Axes aligned with X, Y or Z are colored red, green or blue, respectively. Intermediate positions are represented by mixed colors, as indicated on Figures 12 and 13.

It can be clearly seen from the distributions that the experimental axes are of mixed directions at $\varepsilon = 1\%$, and that they rotate toward X–Y directions as strain accumulates, which is consistent with previous results (Figure 9). The simulated axes have similar X–Y directions at all deformations. In both experiment (at the largest strains) and simulation (at all strains), the preferential direction axes tend to be perpendicular to the tensile direction (Z) and to the X–Y component of the orientation vector. For example, orientations with a dominant X component (in Rodrigues space) have a preferential axis along Y, and, similarly, orientations with a dominant Y component (in Rodrigues space) have a preferential axis along X. This trend is global, and the regions about the Z ∥ ⟨1 0 0⟩, Z ∥ ⟨1 1 0⟩ and Z ∥ ⟨1 1 1⟩ fibers (shown on Figure 11) do not show any particularity.

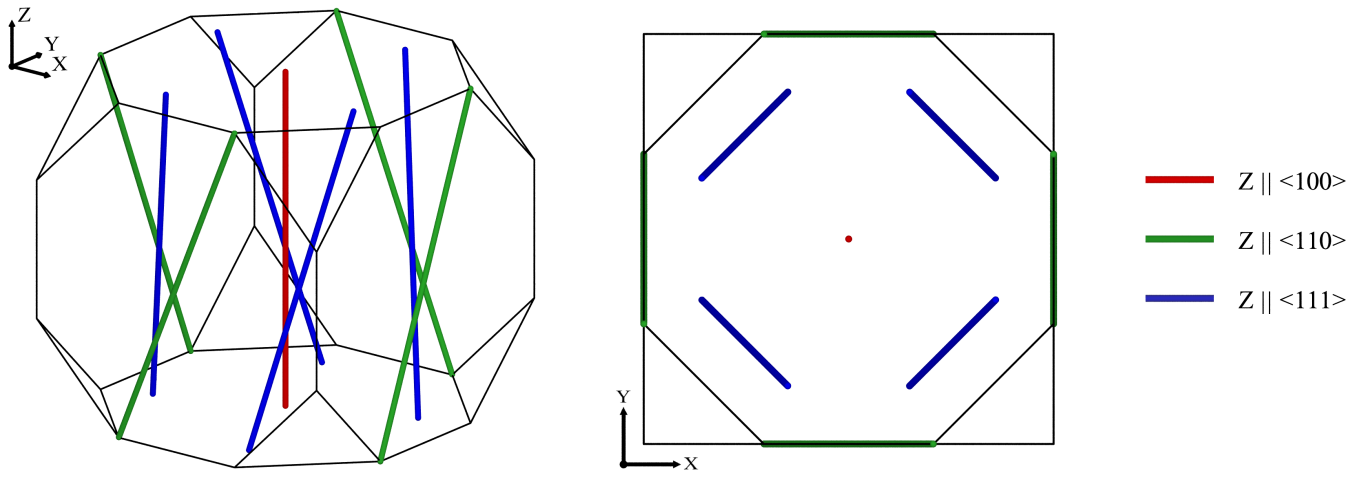

Figure 11: Ideal fibers for uniaxial tension (along Z) on an FCC polycrystal (Z ∥ ⟨1 0 0⟩, ⟨1 1 0⟩ and ⟨1 1 1⟩, which correspond to the three vertices of the standard triangle). Perspective and Z views.

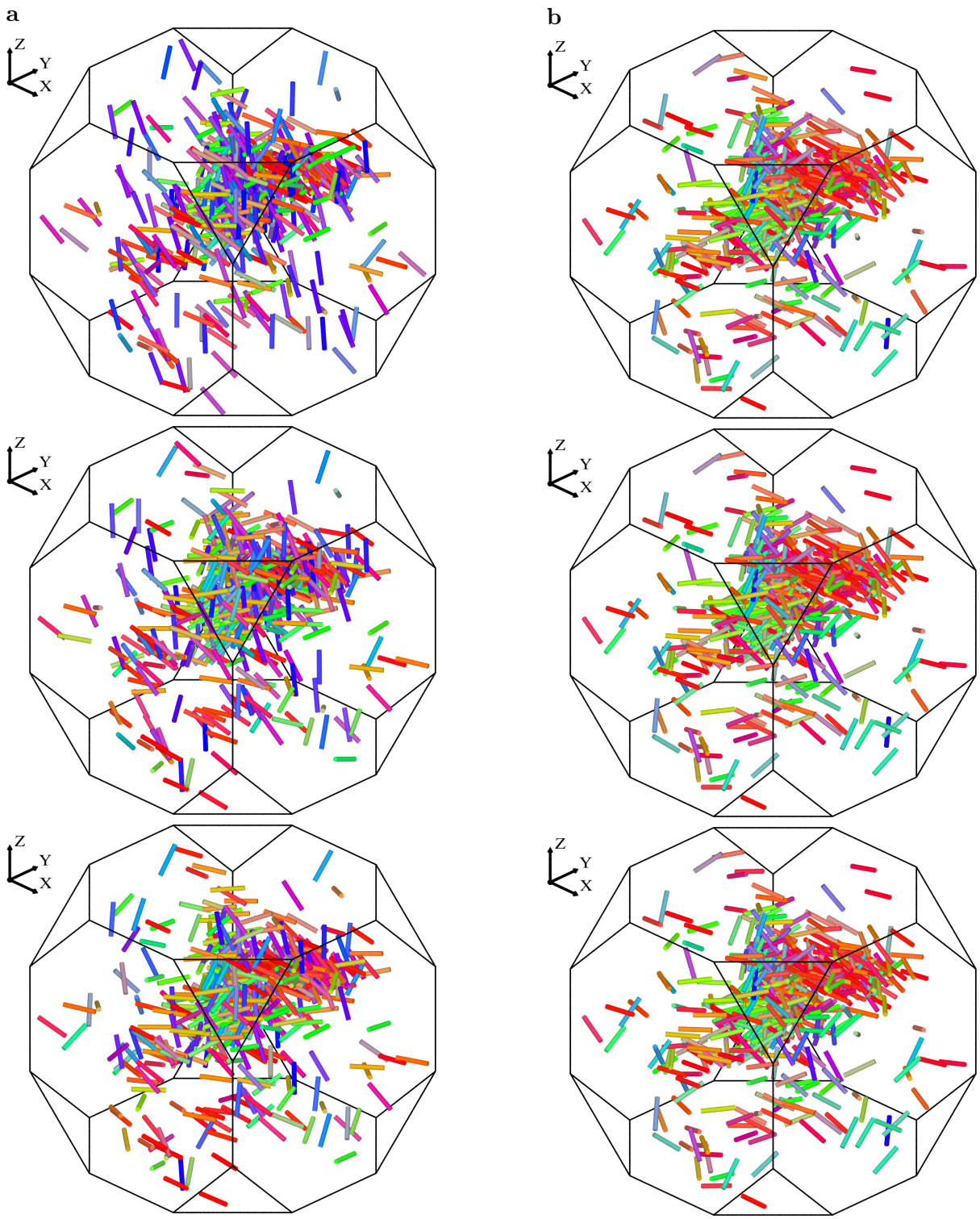

Figure 12: Correlation between the preferential disorientation axes and the average orientations of the grains, illustrated in the Rodrigues fundamental region (perspective view), for (a) experiment and (b) simulation. For each grain, the preferential disorientation axis is represented as a baton located at the average orientation of the grain. The color of the axis is related to its direction following the color key. From top to bottom, $\varepsilon = 1$, 1.5, 2, 2.5 and 4.5%, successively.

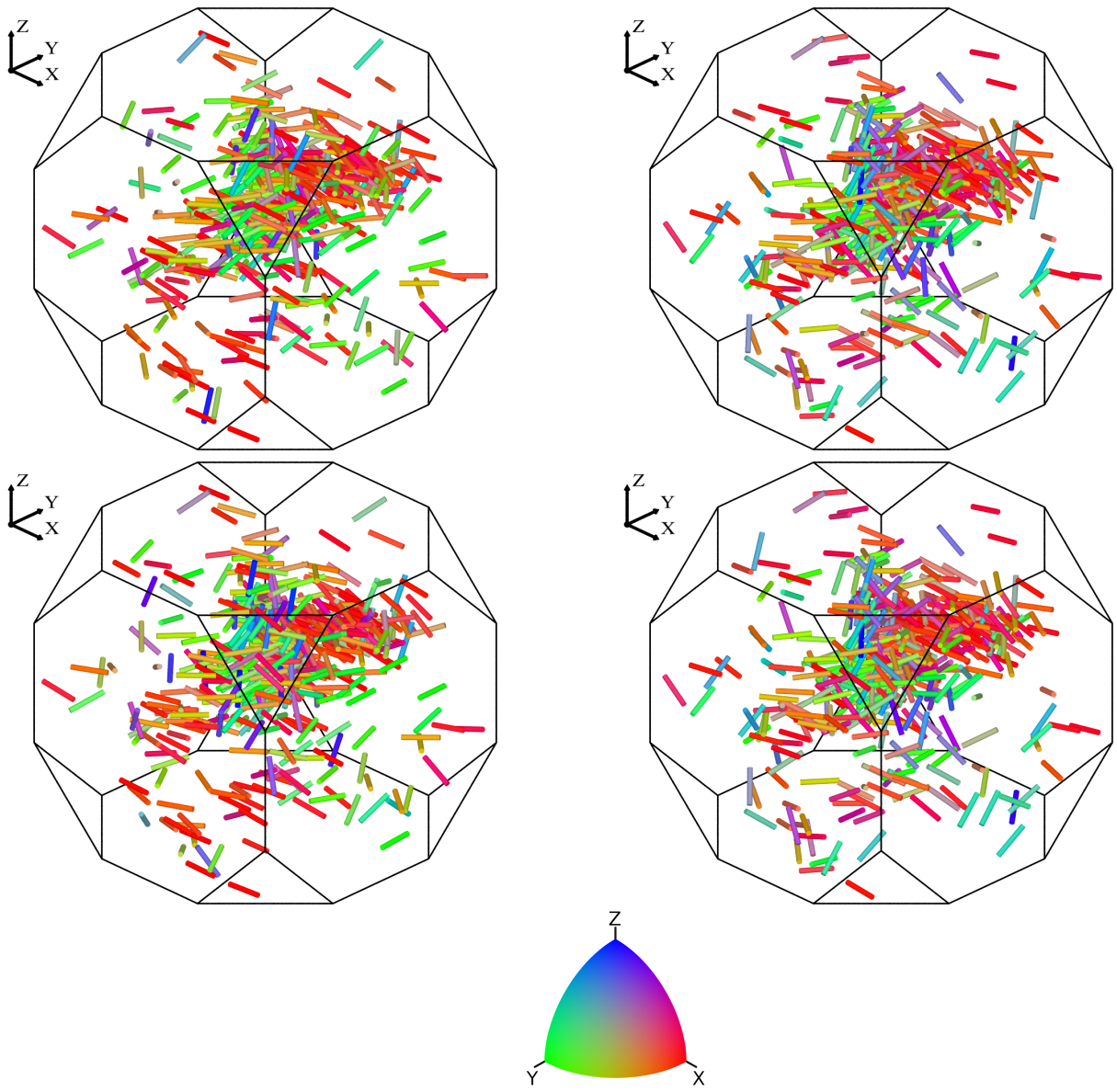

Figure 12: (continued)

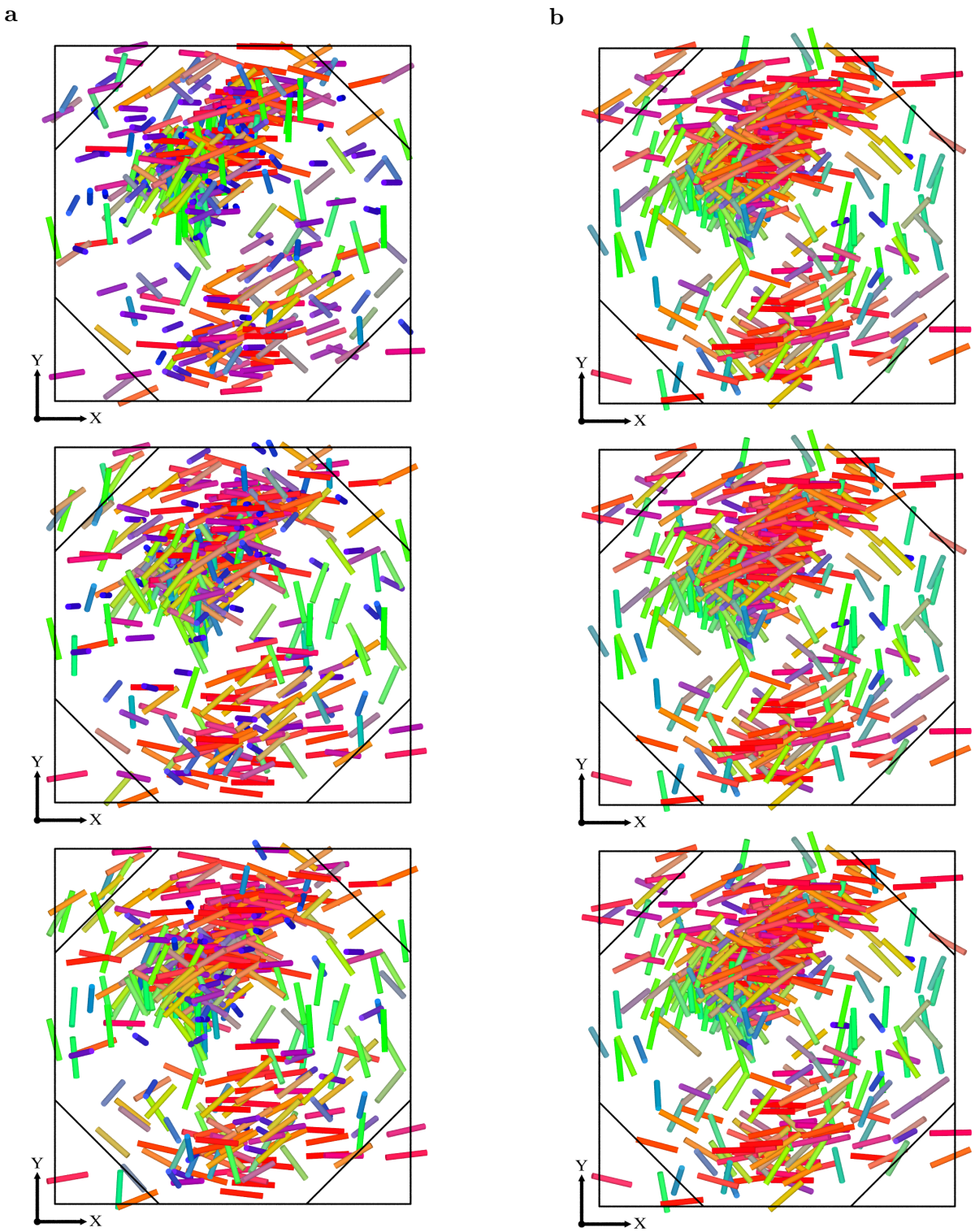

Figure 13: Correlation between the preferential disorientation axes and the average orientations of the grains, illustrated in the Rodrigues fundamental region (Z view), for (a) experiment and (b) simulation. For each grain, the preferential disorientation axis is represented as a baton located at the average orientation of the grain. The color of the axis is related to its direction following the color key. From top to bottom, $\varepsilon = 1$, 1.5, 2, 2.5 and 4.5%, successively.

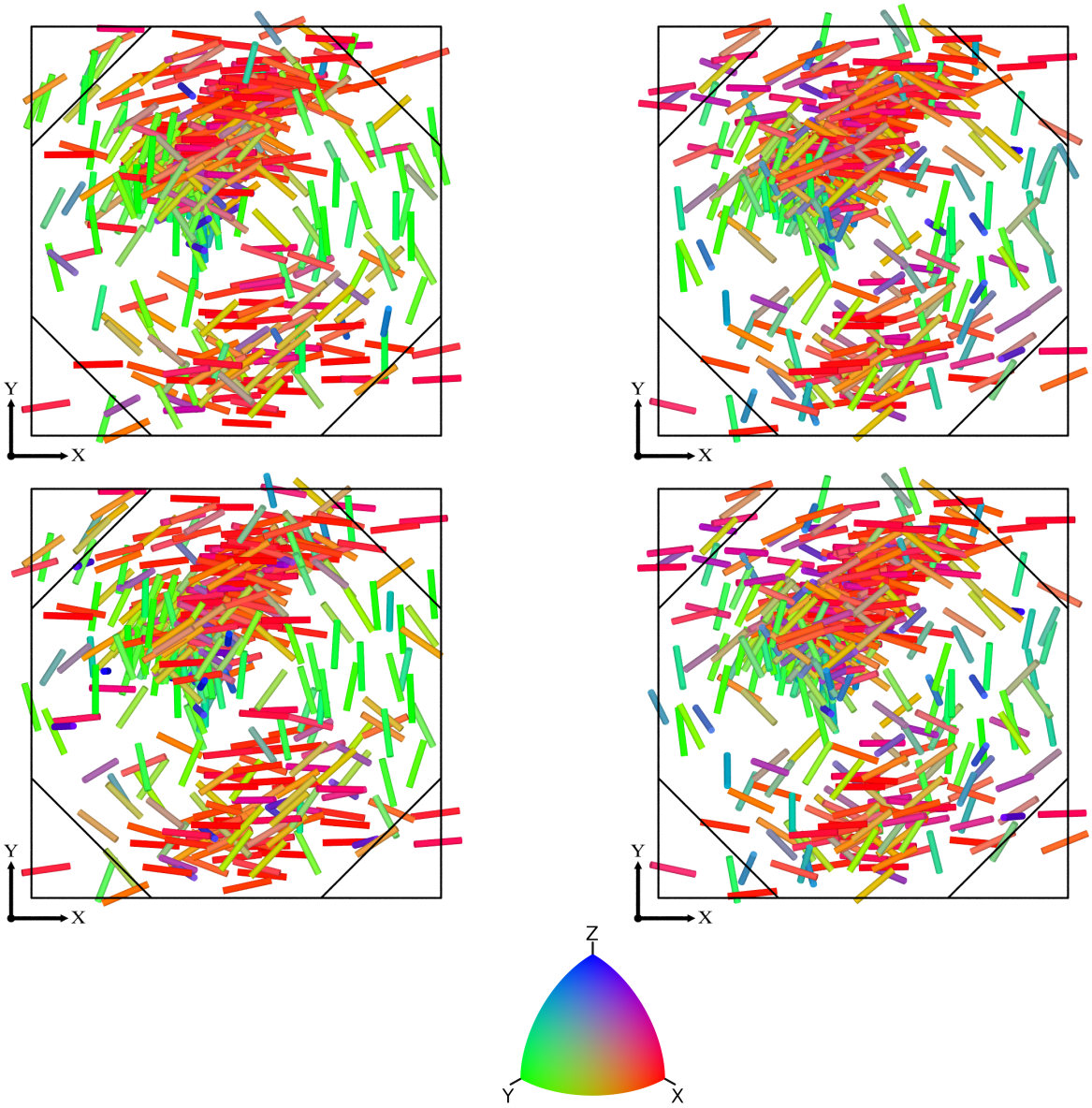

Figure 13: (continued)

5 Discussion

A set of 466 grains was used to analyse the evolution of the anisotropy properties of their orientation distributions, which can be considered as statistically significant [41]. Different metrics were used to describe the anisotropy properties of the orientation distributions, for which experiment and simulation show different degrees of agreement. The preferential disorientation axis, in particular, appear to be particularly interesting, as it is an important attribute of the orientation distribution and shows quite clear dependency on orientation. In both experiment and simulation, the preferential disorientation axes distribute perpendicular to the tensile direction (Z) and perpendicular to the X–Y component of the orientation vector. In experiment, this develops progressively with strain. The appreciable agreement on the preferential disorientation axis between experiment and simulation, including grain by grain, allows for more detailed analysis of their relationship to the deformation mechanisms. In Ref. [4], such an analysis was carried out for hot plane strain compression, and a mechanics-based model for the development of an anisotropic orientation distribution was proposed. Following a similar approach, the simulation results are first used to relate the preferential disorientation axes to the slip geometry (Section 5.1), and the simplified model is used and extended to investigate the role of the stress distribution (Section 5.2).

5.1 Slip geometry and variability

In a grain, plastic deformation occurs by activation of slip on specific systems (among $\{1\,1\,1\}\langle 1\,1\,0\rangle$). Slip on a specific system generates lattice rotation about its spin vector, $\boldsymbol{t}^\alpha = \boldsymbol{m}^\alpha \times \boldsymbol{s}^\alpha$, where $\boldsymbol{m}^\alpha$ is the slip plane normal and $\boldsymbol{s}^\alpha$ is the slip direction. It follows that a variation of slip on a system generates a variation of lattice rotations about its spin vector ($\boldsymbol{t}^\alpha$), which finally leads to a 1-D orientation distribution along the spin vector ($\boldsymbol{t}^\alpha$). The simultaneous activation of several systems generates lattice rotation variations about spin vectors of different directions, which finally leads to a general, 3-D orientation distribution. However, as the systems showing the larger slip variations produce the larger rotation variations, the 3-D orientation distribution is anisotropic and preferentially elongated along the spin vectors of these systems. The orientation distribution of a grain therefore depends on the slip activity (and heterogeneity) inside the grain, and therefore holds a certain degree of information on it.

The slip activity inside the grains of the polycrystal can be investigated from the elemental slip rates. As the focus is on the distributions of orientations, the slip rates are also considered in terms of distribution (over all elements), with no consideration to their spatial locations within the grain. Values at the final strain ($\varepsilon = 4.5\%$) are considered, but considering other strains (or even the slips at final strain) would provide similar results, as the simulated preferential disorientation axes are largely independent of strain (see Figures 9b, 12b and 13b). To determine what are the characteristic directions ($\boldsymbol{m}^\alpha$, $\boldsymbol{s}^\alpha$ and $\boldsymbol{t}^\alpha$) of the most active slip systems, the characteristic directions of all systems are weighted by the corresponding average absolute slip rates, $|\overline{\dot{\gamma}^\alpha}|$, and their distributions over all grains are analysed. For each grain, the average values of the characteristic directions, $\overline{\boldsymbol{m}^\alpha}$, $\overline{\boldsymbol{s}^\alpha}$ and $\overline{\boldsymbol{t}^\alpha}$, are used (12 values per grain). The distributions of $|\overline{\dot{\gamma}^\alpha}|\,\overline{\boldsymbol{m}^\alpha}$, $|\overline{\dot{\gamma}^\alpha}|\,\overline{\boldsymbol{s}^\alpha}$ and $|\overline{\dot{\gamma}^\alpha}|\,\overline{\boldsymbol{t}^\alpha}$ over all grains are provided in Figure 14. Both the slip plane normals ($\overline{\boldsymbol{m}^\alpha}$) and slip directions ($\overline{\boldsymbol{s}^\alpha}$) are distributed at about 45° from the tensile direction (Z), and the spin vectors ($\overline{\boldsymbol{t}^\alpha}$) have X–Y directions, i.e. are perpendicular to the tensile direction (Z). These characteristics correspond to those of the systems of maximal Schmid factors for uniaxial tension.

The slip rate variability on a specific system of a grain is quantified as the standard deviation of the slip rates of all elements (considering, as before, the values at $\varepsilon = 4.5\%$). The slip rate variabilities are plotted against the (absolute) slip rates on Figure 15. It is clear that the systems of high slip rates exhibit that higher slip rate variability. The higher slip rate variabilities of the most active slip systems combined with their spin vectors being perpendicular to the tensile direction lead to the (experimental and simulated) preferential disorientation axis distributions perpendicular to the tensile direction (see Figure 9). The dependency of the variability of slip rate on the (absolute) average slip rate only applies to first order, however, as significant

scatter also exists on Figure 15: systems of similar average slip rates may exhibit significantly different slip rate variabilities or, equivalently, similar slip rate variabilities can be observed for systems of different slip rates (this was also observed for higher strain rate sensitivity [4]). So, the (absolute) average slip rate and slip rate variability on a slip system also depend on the conditions that the system (and the grain) locally undergoes, especially in terms of the local stress and stress heterogeneity, which depends not only on the grain orientation but also on grain interaction.

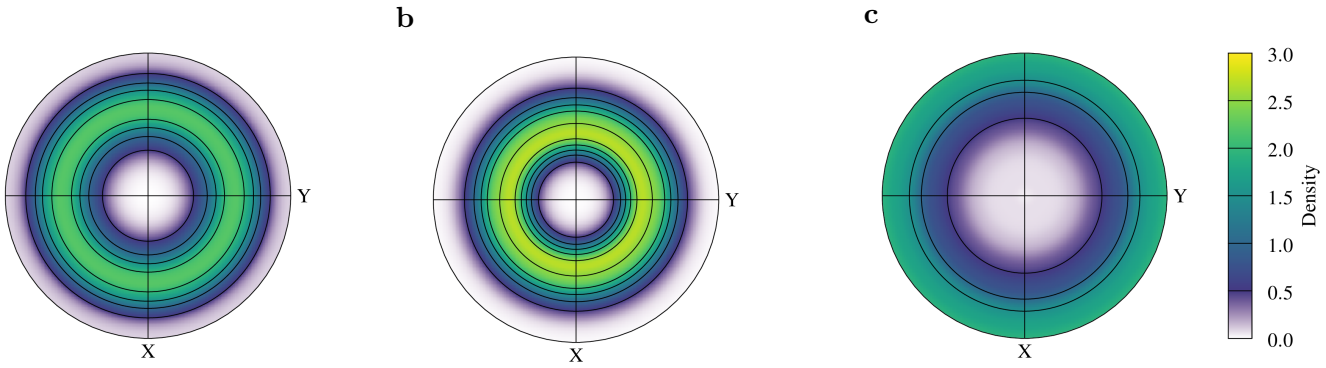

Figure 14: Geometry of the active slip systems for the 466 grains in simulation. Distributions of (a) $|\overline{\dot{\gamma}^{\alpha}}|\,\overline{\boldsymbol{m}^{\alpha}}$, (b) $|\overline{\dot{\gamma}^{\alpha}}|\,\overline{\boldsymbol{s}^{\alpha}}$ and (c) $|\overline{\dot{\gamma}^{\alpha}}|\,\overline{\boldsymbol{t}^{\alpha}}$ in simulation (equal-area projections). Uniaxial symmetry is applied. For clarity, the discrete data (12 slip systems $\times$ 466 grains) are omitted to show only their distributions.

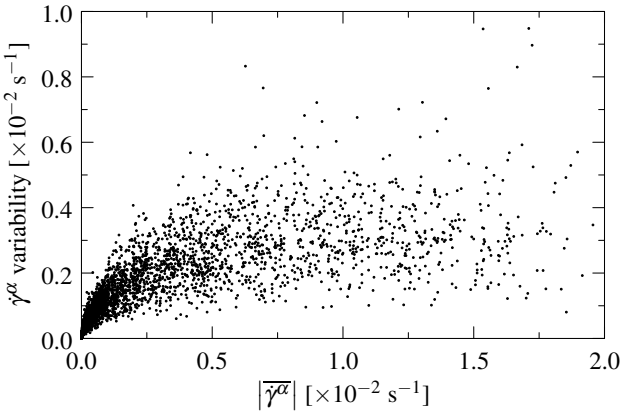

Figure 15: Relation between the slip rate variability and the average slip rate. The data are plotted for the 12 slip systems of each of the 466 grains in simulation.

5.2 *Influence of the stress distribution*

The lattice reorientation rate depends on the slip rates on the slip systems, which are themselves related to the resolved shear strengths (Equation 7) and, hence, to the stress. In the grains of a polycrystal, stress variation develops as a result of grain interaction. Under the assumption of zero (or negligible) local rigid-body rotation, the dependence of lattice reorientation on stress is given by

$$\frac{\partial \dot{\boldsymbol{r}}^*}{\partial \sigma_v} = -\sum_\alpha \frac{\partial \dot{\gamma}^\alpha}{\partial \tau^\alpha} \left(\boldsymbol{t}^\alpha \otimes \boldsymbol{p}^\alpha\right), \tag{14}$$

where $\boldsymbol{\sigma}_v$ is the stress written in vector form [4]. The partial derivative is known from the kinetics expression given by Equation 7,

$$\frac{\partial \dot{\gamma}^\alpha}{\partial \tau^\alpha} = \frac{\dot{\gamma}_0}{m\, g^\alpha} \left|\frac{\tau^\alpha}{g^\alpha}\right|^{\frac{1}{m}-1}, \tag{15}$$

or, in terms of slip rate $\dot{\gamma}^\alpha$,

$$\frac{\partial \dot{\gamma}^\alpha}{\partial \tau^\alpha} = \frac{\dot{\gamma}_0}{m\, g^\alpha} \left|\frac{\dot{\gamma}^\alpha}{\dot{\gamma}_0}\right|^{1-m}. \tag{16}$$

For usual values of m in the range 0.02–0.15 (here 0.03), it is a strongly increasing function of τ^α and a nearly linear function of $\dot{\gamma}^\alpha$. The factor $(\boldsymbol{t}^\alpha \otimes \boldsymbol{p}^\alpha)$, where $\boldsymbol{t}^\alpha$ is (as before) the spin vector, $\boldsymbol{p}^\alpha$ is the symmetrical Schmid tensor written in vector form and $\otimes$ is the dyadic product between vectors, is fully geometrical and depends only on the crystal lattice orientation. Following Equations (14)–(16), the most active slip systems have a greater contribution to $\partial \dot{\boldsymbol{r}}^*/\partial \sigma_v$, according to the $\partial \dot{\gamma}^\alpha/\partial \tau^\alpha$ factor.

By definition, $\partial \dot{\boldsymbol{r}}^*/\partial \sigma_v$ provides the variation of the reorientation velocity vector as a function of a variation of the stress vector, and so the stress distribution inside a grain generates a reorientation distribution (and finally an orientation distribution) depending on $\partial \dot{\boldsymbol{r}}^*/\partial \sigma_v$ (Equation 14). This expression can be subjected to a singular value decomposition,

$$\frac{\partial \dot{\boldsymbol{r}}^*}{\partial \sigma_v} = \boldsymbol{U}\, \boldsymbol{S}\, \boldsymbol{V}^T, \tag{17}$$

where $\boldsymbol{U}$ is a (3, 3) orthogonal tensor, $\boldsymbol{S}$ is a (3, 6) diagonal tensor, and $\boldsymbol{V}$ is a (6, 6) orthogonal tensor. The diagonal entries of $\boldsymbol{S}$ are sorted in decreasing order. It is important to note that $\boldsymbol{U}$ is a basis of the physical (real) space and $\boldsymbol{V}$ is a basis of the stress space.

A Taylor (iso-strain) assumption was used in Ref. [4] to compute the nominal stress, slip rates and value of $\partial \dot{\boldsymbol{r}}^*/\partial \sigma_v$. A random, isotropic stress distribution (random vectors in stress space) was then considered, which leads to a reorientation velocity distribution of principal directions given by the rows of $\boldsymbol{U}$ and magnitudes given by the associated diagonal entries of $\boldsymbol{S}$. Note that the resulting distribution will necessarily show greater orientation dependency than the experimental or simulated ones, as the preferential disorientation axes depend only on orientation. The distribution of the preferential disorientation axis resulting from these assumptions is provided in Figure 16. It can be seen that the equal-area projection is in good agreement with the experimental and simulated ones (see e.g. Figure 9a,b at $\varepsilon = 4.5\%$), but that the distribution in orientation space (Figure 16b versus Figures 12 and 13) shows less agreement (while good agreement was obtained for hot plane strain compression [4]). Specifically, considering an idealized configuration consisting of a Taylor stress and an isotropic stress distribution does not reproduce the distribution of the preferential disorientation axes in a region surrounding the $Z \| \langle 1\,0\,0 \rangle$ fiber where the axes are oriented parallel (rather than perpendicular) to the X–Y component of the orientation vector.

Given that the idealized configuration does not fully reproduce the observed (experimental or simulated) orientation dependency of the preferential disorientation axes, the following question arises: what is (or are) the driving factor(s) for the difference (especially around $Z \| \langle 1\,0\,0 \rangle$), in terms of the assumptions made in the idealized configuration? As per the specificities of the idealized configuration, the two main factors may be: *(1)* the assumption of iso-strain (Taylor model) to compute the nominal stress and $\partial \dot{\boldsymbol{r}}^*/\partial \sigma_v$, and *(2)*

the assumption of an isotropic stress distribution to compute the preferential disorientation axes. Another possible factor is *(3)* the assumption of zero (or negligible) local rigid-body rotation, which, based on the analysis made in Section 5.1, should not play an important role, but is also considered in the following for completeness.

The procedure to determine the relative influences of the three main assumptions is to consider the idealized configuration and relax each assumption independently, as follows:

1. Relaxed iso-strain assumption: the finite-element average stress is considered in place of the Taylor stress. This provides a new value of $\partial\dot{\boldsymbol{r}}^*/\partial\sigma_v$, from which the preferential disorientation axis of the grain is computed as previously, by singular value decomposition (Equation 17).

2. Relaxed isotropic-stress-distribution assumption: the (discrete, anisotropic) finite-element stress distribution is considered instead of the ideal isotropic distribution. So, the nominal value of $\partial\dot{\boldsymbol{r}}^*/\partial\sigma_v$ is still used, but the finite-element stress vectors (with respect to the average stress) are then multiplied by $\partial\dot{\boldsymbol{r}}^*/\partial\sigma_v$ to obtain the corresponding (discrete) reorientation rate distribution, from which the preferential disorientation axis is computed as for the simulation results, using Equation 11.

3. Relaxed zero-spin assumption: the (discrete, anisotropic) finite-element spin rate distribution is introduced. The finite-element spin rate vectors (with respect to the average spin) are combined with the reorientation rate vectors resulting from the isotropic stress distribution as per the standard composition [4] to obtain a new reorientation rate distribution, whose anisotropy properties are computed as in the simulation, using Equation 11 (due to the discrete nature of the spin rates, the isotropic stress distribution is also considered as discrete, as in configuration 2).

Figure 17 provides the preferential disorientation axes obtained in the three configurations, as equal-area projections and distributions in orientation space (to be compared to Figures 9, 12 and 13 at $\varepsilon = 4.5\%$). In addition, the correlation to the experimental disorientation axes ($\boldsymbol{v}_{\mathbf{1}}^{\mathrm{exp}}$) is quantified as the average value of the angles between the experimental and predicted axes (same metric as in Figure 10). The values are 46° for the idealized configuration (iso-strain and isotropic stress distribution), and 38°, 56° and 47° for the three successive relaxed configurations (37° for the finite element simulation). It is clear from these results that considering the finite-element average stresses instead of the Taylor stresses (configuration 1) largely corrects the preferential disorientation axes in the $Z\|\langle 1\,0\,0\rangle$ region, and gives a degree of agreement very close to the experiment–simulation one. Conversely, considering an anisotropic stress distribution or a non-zero spin distribution (alone) does not improve the distribution. This can be explained by several reasons. First, good results with an isotropic stress distribution (configuration 1) indicate that the preferential disorientation axes are controlled by the shape of $\partial\dot{\boldsymbol{r}}^*/\partial\sigma_v$ rather than by the shape of the stress distribution. $\partial\dot{\boldsymbol{r}}^*/\partial\sigma_v$ depends on the crystal orientation, (non-linearity of the) slip law, and average stress of the grain, which ensures proper selection of the active slip systems. Second, the lack of improvement when considering the actual stress distribution (variations about the average) can be related to the fact that it is not considered about the correct nominal stress. Finally, the spin, as not being intrinsically associated to particular spatial directions (unlike slip), does not involve a particular distribution of the associated reorientation directions.

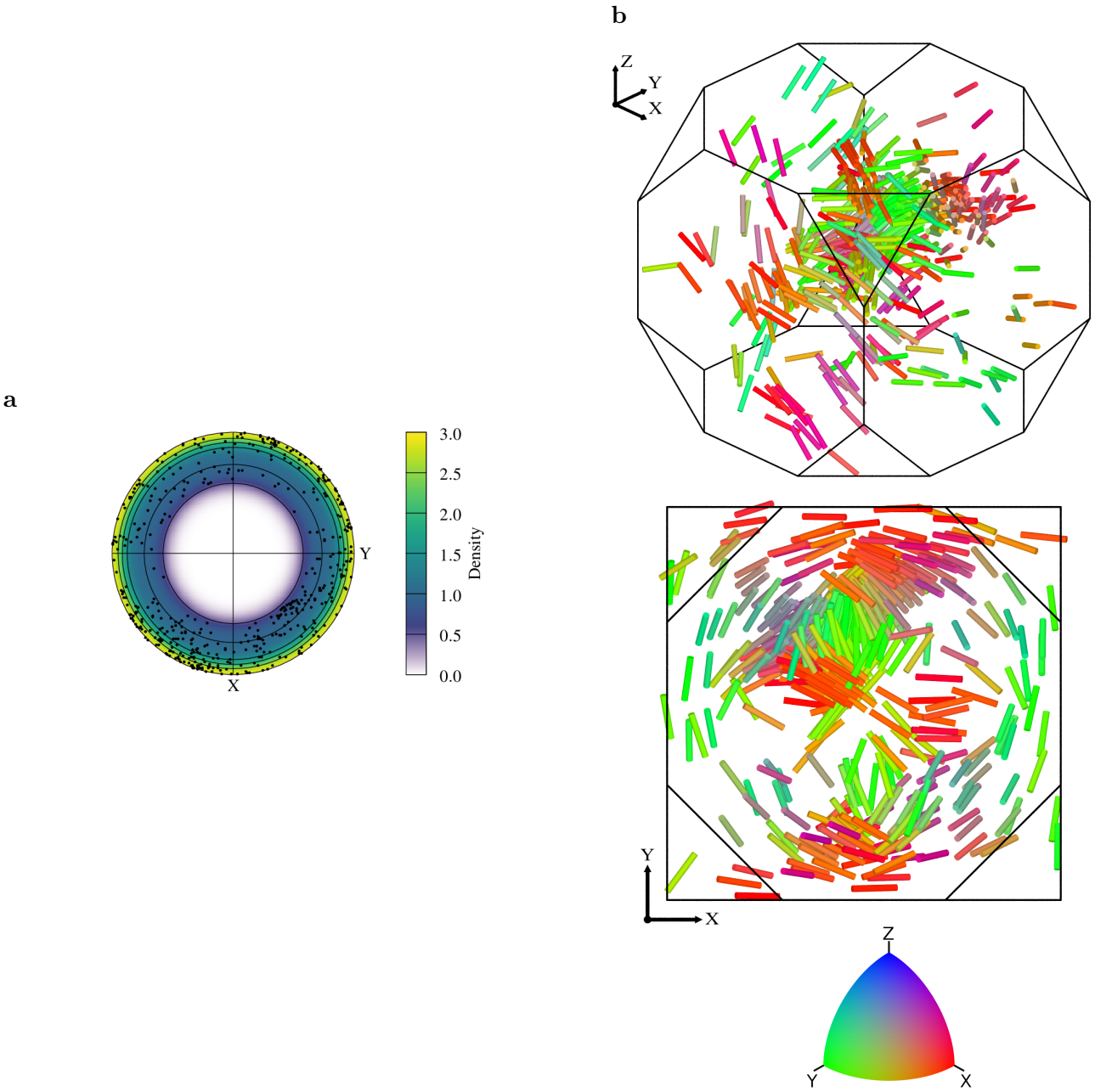

Figure 16: Preferential disorientation axes resulting from an isotropic stress variability shown as (a) distribution over all orientations (equal-area projections) and (b) correlation with the associated average orientations.

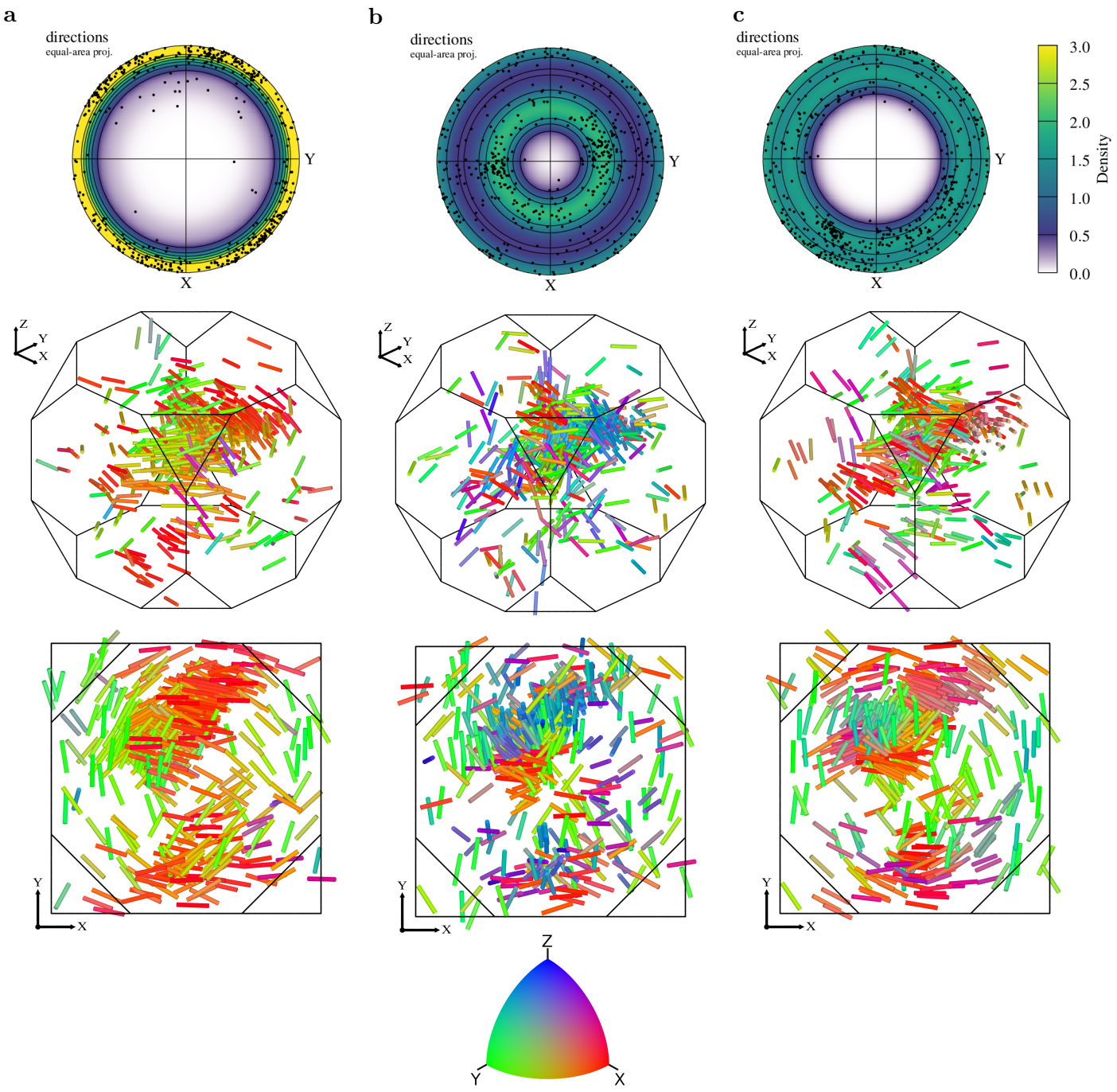

Figure 17: Preferential disorientation axes resulting from the idealized configuration and (a) the relaxed iso-strain assumption, (b) the relaxed isotropic-stress-distribution assumption and (c) the relaxed zero-spin assumption.

6 Conclusions

The orientation distributions developing within individual grains of an aluminium polycrystal deformed in tension were experimentally characterized by far-field 3D X-ray diffraction microscopy and simulated using the finite-element method. A statistically significant set of 466 grains was considered. In the experiment, a method was presented to unambiguously determine the anisotropy properties of the orientation distributions from the broadening of the diffraction spots. In the simulation, each grain was discretized into several hundreds of elements, also giving access to intra-grain orientation distributions. The anisotropy properties of the orientation distributions were analysed in terms of angular extent (average disorientation angle, $\bar{\theta}$), anisotropy factor (θ_a) and preferential disorientation axis ($\boldsymbol{v_1}$). A high degree of variability of the results was found among grains both in experiment and simulation. The average disorientation angles were found to increase almost linearly with strain and to be in appreciable agreement between experiment and simulation, although evolving faster in simulation. The anisotropy intensity was found to remain similar during deformation, with typical values in the range 1.5–3, with only a slow increase with strain in experiment. The preferential disorientation axes were found to be mainly oriented perpendicular to the tensile direction (Z) and perpendicular to the X–Y component of the Rodrigues orientation vector. Here, experiment and simulation are in good agreement. An analysis based on the simulation results revealed that the development of preferential disorientation axes can be explained by larger slip variations developing on the most active slip systems. Using a simplified approach, it was possible to show that an accurate estimate of the (average) stress is essential to properly predict the preferential disorientation axis, especially for orientations about the Z $\parallel \langle 1\,0\,0 \rangle$ fiber, which is properly done by the finite-element simulation. The intra-grain stress distribution (about the average) has comparatively less influence and can be assumed as isotropic to first order.

7 Acknowledgments

The experimental and simulation results of this research were obtained principally by LR in collaboration with RQ while LR was a Ph.D candidate at Mines Saint-Étienne and constitute part of his dissertation. Additional analyses were then carried out by RQ. The authors acknowledge W. Ludwig, J. Wright and A. Borbély for help during the experiment at ESRF. One of the author (RQ) warmly thanks Paul Dawson for his comments on an early version of the manuscript.

A Orientation weights and texture correction

In the presence of a preferential grain orientation distribution (or (non-random) "texture") in the investigated polycrystal, weights can be defined from the grain orientations and used when computing results over all grains, so that the obtained results are representative of a general, texture-free material. This process is referred to as "texture correction".

Under uniaxial sample symmetry, orientations can be plotted on the standard triangle (inverse pole figure), where each orientation is represented by a unique point corresponding to the position of the tensile axis in the crystal coordinate system. For each orientation, a weight can then be defined from the fraction of all possible orientations (all positions of the standard triangle) the orientation represents. This is done by Voronoi tessellation, by which each orientation generates a cell that correspond to the region that is closer to the orientation than to any other orientation. The weight of an orientation is then defined as the (relative) surface area of its associated Voronoi cell. (Equal-area projection is considered for the inverse pole figure, so that the surface areas of the orientation cells are not biased by the projection itself.) The more orientation are "clustered", the smaller their weights; conversely, the more "isolated" an orientation is, the larger its weight. For a texture-free material, all orientations have (roughly) equal surface areas.

The resulting tessellation is provided in Figure 18a, and the (normalized) surface areas of the orientations vary from 0.07 to 8, while 90% range from 0.2–2.5. As expected, smaller (normalized) surface areas are

obtained for orientations where the ODF is larger (compare Figures 18a and 1d). The present definition or orientation weights is therefore similar (still generally non-equivalent) to considering the inverse values of the ODF.

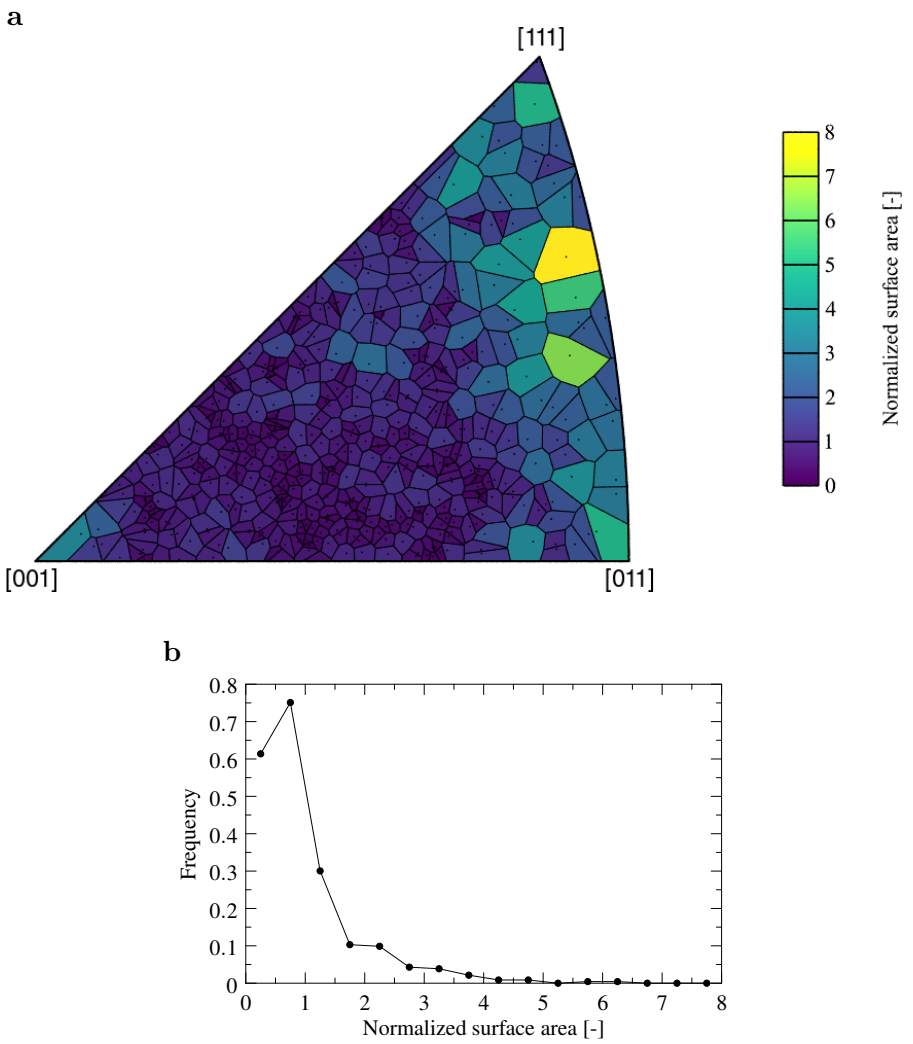

Figure 18: Computation of orientation weights via Voronoi tessellation on the standard triangle (inverse pole figure) under equal-area projection. (a) Voronoi tessellation, where the orientations are represented by the black dots and the Voronoi cells are colored according to their (normalized) surface areas. (b) Distributions of the orientation weights over all grains.

B Computation of the average disorientation angle

For nD isotropic, normal disorientation distributions, the expression of the average disorientation angle ($\bar{\theta}$) as a function of the standard deviation of the normal distribution in one direction (n), is given by [5]

$$\bar{\theta} \simeq C(n)\,\sigma, \tag{18}$$

where

$$C(n) = \sqrt{2}\,\frac{\Gamma\left[(n+1)/2\right]}{\Gamma\left(n/2\right)}, \tag{19}$$

which yields

$$C(1) = \sqrt{2/\pi} \quad < \quad C(2) = \sqrt{\pi/2} \quad < \quad C(3) = 2\sqrt{2/\pi}. \tag{20}$$

For a 3D anisotropic disorientation distribution, the expression of the average disorientation angle ($\bar{\theta}$) must involve the standard deviations of the normal distributions in the three principal directions (θ_1, θ_2 and θ_3). The scaling factors of nD isotropic distributions given in Equation 20 ($C(\bullet)$) also applies to the special cases of 3D anisotropic distributions of standard deviations *(i)* $\theta_1 = \sigma$, $\theta_{2,3} = 0$ (for $C(1)$), *(ii)* $\theta_{1,2} = \sigma$, $\theta_3 = 0$ (for $C(2)$) and *(iii)* $\theta_{1,2,3} = \sigma$ (for $C(3)$) and can be considered as reference values to be reproduced (or closely approximated) by any expression of $\bar{\theta}$ generalized to the anisotropic case. We propose an expression proportional to the L^p-norm of the (θ_1, θ_2, θ_3) vector:

$$\bar{\theta} = a \, \left({\theta_1}^p + {\theta_2}^p + {\theta_3}^p\right)^{\frac{1}{p}} . \tag{21}$$

The values of a and p can be determined by comparing the $\bar{\theta}$ values provided by Equations 18 and 21 for different values of n (to first order, and knowing that the problem is overdetermined). Considering $n = 1$, we get $a = C(1) = \sqrt{2/\pi}$. Then, following simple mathematical manipulations, $n = 2$ yields $p = \ln(2)/\ln(\pi/2) \simeq 1.535$ while $n = 3$ yields $p = \ln(3)/\ln(2) \simeq 1.585$. The similar values of p obtained for $n = 2$ and $n = 3$ (both of which would also apply to $n = 1$), which correspond to extremal values of θ_i (in their respective domains of definition), show that the expression of $\bar{\theta}$ provided by Equation 21 can be appropriately used. An "optimal" value of p can be obtained by fitting Equation 21 to data obtained from numerical experiments. To do so, θ_2 and θ_3 were varied over their respective domains of definition ($\theta_2 \in [0, \theta_1]$ and $\theta_3 \in [0, \theta_2]$), and, for each value, 10^6 data points were generated following the corresponding 3-variate normal distribution, and the actual value of $\bar{\theta}$ was computed. The data are shown on Figure 19, and the identification provided $p = 1.58$. It is clear from Figure 19 that Equation 21 with $a = \sqrt{2/\pi}$ and $p = 1.58$ closely approximates the numerical values. The average error is 0.32% and the maximum error is 1.2%.

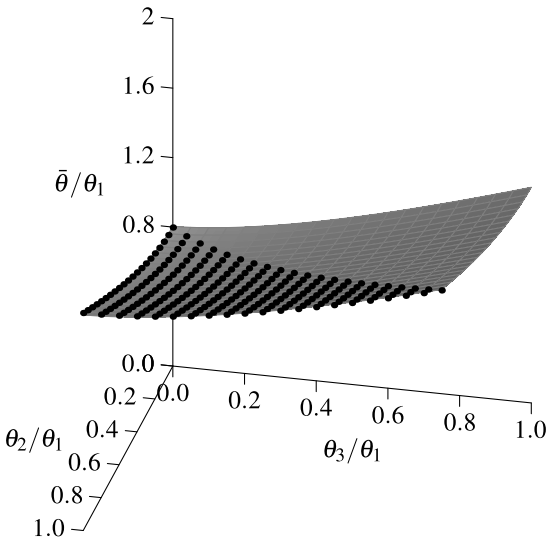

Figure 19: Relation between the average disorientation angle ($\bar{\theta}$) and the standard deviations about the principal disorientation axes (θ_1, θ_2 and θ_3). The dots represent the numerical values, and the surface represents the analytical approximation.

References

[1] N. Hansen. New discoveries in deformed metals. *Metall. Mater. Trans. A*, 32A:2917–2935, 2001.

[2] F.J. Humphreys. Modelling mechanisms and microstructures of recrystallisation. *Mater. Sci. Tech.*, 8:135–143, 1992.

[3] R. Quey, G.-H. Fan, Y. Zhang, and D. Juul Jensen. Importance of deformation-induced local orientation distributions for nucleation of recrystallization. *Acta Mater.*, 210:116808, 2021.

[4] R. Quey, J.H. Driver, and P.R. Dawson. Intra-grain orientation distributions in hot-deformed aluminium: orientation dependence and relation to deformation mechanisms. *J. Mech. Phys. Solids*, 84:506–27, 2015.

[5] J.-Ch. Glez and J.H. Driver. Orientation distribution analysis in deformed grains. *J. Appl. Crystallogr.*, 34:280–288, 2001.

[6] J.-Ch. Glez and J.H. Driver. Substructure development in hot plane strain compressed Al-1%Mn crystals. *Acta Mater.*, 51:2989–3003, 2003.

[7] W. Pantleon, W. He, T.P. Johansson, and C. Gundlach. Orientation inhomogeneities within individual grains in cold-rolled aluminium resolved by electron backscatter diffraction. *Mater. Sc. Eng., A*, 483-484:668–671, 2008.

[8] S. Panchanadeeswaran, R.D. Doherty, and R. Becker. Direct observation of orientation change by channel die compression of polycrystalline aluminum–use of a split sample. *Acta Mater.*, 44:1233–1262, 1996.

[9] C.C. Merriman, D.P. Field, and P. Trivedi. Orientation dependence of dislocation structure evolution during cold rolling of aluminum. *Mater. Sc. Eng., A*, 494:28–35, 2008.

[10] R. Quey, D. Piot, and J.H. Driver. Microtexture tracking in hot-deformed polycrystalline aluminium: experimental results. *Acta Mater.*, 58:1629–1642, 2010.

[11] E.B. Marin and P.R. Dawson. On modelling the elasto-viscoplastic response of metals using polycrystal plasticity. *Comput. Methods Appl. Mech. Eng.*, 165:1–21, 1998.

[12] E.B. Marin and P.R. Dawson. Elastoplastic finite element analyses of metal deformations using polycrystal constitutive models. *Comput. Methods Appl. Mech. Eng.*, 165:23–41, 1998.

[13] R. Quey and M. Kasemer. The Neper/FEPX Project: free / open-source polycrystal generation, deformation simulation, and post-processing. *IOP Conf. Ser.: Mater. Sci. Eng.*, 1249:012021, 2022.

[14] R. Quey, P.R. Dawson, and J.H. Driver. Grain orientation fragmentation in hot-deformed aluminium: experiment and simulation. *J. Mech. Phys. Solids*, 60:509–24, 2012.

[15] H.F. Poulsen. *Three Dimensional X-Ray Diffraction Microscopy*. Springer, 2004.

[16] L. Margulies, G. Winther, and H.F. Poulsen. In situ measurement of grain rotation during deformation of polycrystals. *Science*, 291:2392, 2001.

[17] H.F. Poulsen, L. Margulies, S. Schmidt, and G. Winther. Lattice rotations of individual bulk grains: part I: 3D X-ray characterization. *Acta Mater.*, 51:3821–30, 2003.

[18] G. Winther, L. Margulies, S. Schmidt, and H.F. Poulsen. Lattice rotations of individual bulk grains: part II: correlation with initial orientation and model comparison. *Acta Mater.*, 52:2863–2872, 2004.

[19] W. Ludwig, A. King, P. Reischig, M. Herbig, E.M. Lauridsen, S. Schmidt, H. Proudhon, S. Forest, P. Cloetens, S. Rolland du Roscoat, J.Y. Buffière, T.J. Marrow, and H.F. Poulsen. New opportunities for 3D materials science of polycrystalline materials at the micrometre lengthscale by combined use of X-ray diffraction and X-ray imaging. *Mater. Sci. Eng. A*, 524:69–76, 2009.

[20] N. Viganò, W. Ludwig, and K.J. Batenburg. Reconstruction of local orientation in grains using a discrete representation of orientation space. *Journal of Applied Crystallography*, 47:1826–1840, 2014.

[21] R.M. Suter, D. Hennessy, C. Xiao, and U. Lienert. Forward Modeling Method for Microstructure Reconstruction Using X-ray Diffraction Microscopy: Single Crystal Verification. *Rev. Sci. Instrum.*, 77:123905, 2006.

[22] R. Pokharel, J. Lind, A.K. Kanjarla, R.A. Lebensohn, S. Fai Li, P. Kenesei, Suter R.M., and A.D. Rollett. Polycrystal plasticity: comparison between grain-scale observations of deformation and simulations. *Annu. Rev. Condens. Matter Phys*, 5:317–46, 2014.

[23] N.Y. Juul, J. Oddershede, A. Beaudoin, K. Chatterjee, M.K.A. Koker, D. Dale, P. Shade, and G. Winther. Measured resolved shear stresses and Bishop-Hill stress states in individual grains of austenitic stainless steel. *Acta Mater.*, 141:388 – 404, 2017.

[24] L. Renversade and R. Quey. Analysis of in-grain orientation distributions in deformed aluminium using X-ray diffraction and finite elements. *9 IOP Conf. Ser.: Mater. Sci. Eng.*, 580:012022, 2019.

[25] C. Hansen, H. Sørensen, Z. Sükösd, and H.F. Poulsen. Reconstruction of Single-Grain Orientation Distribution Functions for Crystalline Materials. *SIAM J. Imaging Sci.*, 2:593–613, 2009.

[26] K.E. Nygren, D.C. Pagan, J.V. Bernier, and M.P. Miller. An algorithm for resolving intragranular orientation fields using coupled far-field and near-field high energy X-ray diffraction microscopy. *Materials Characterization*, 165:110366, 2020.

[27] S.L. Wong, J.-S. Park, M.P. Miller, and P.R. Dawson. A framework for generating synthetic diffraction images from deforming polycrystals using crystal-based finite element formulations. *Comp. Mat. Sc.*, 77:456–66, 2013.

[28] W. Ludwig, A. King, M. Herbig, P. Reischig, J. Marrow, L. Babout, E.M. Lauridsen, H. Proudhon, and Y. Buffière. Characterization of polycrystalline materials by combined use of synchrotron x-ray imaging and diffraction techniques. *J. Microsc.*, 62:22–28, 2010.

[29] N. Gueninchault, H. Proudhon, and W. Ludwig. Nanox: a miniature mechanical stress rig designed for near-field X-ray diffraction imaging techniques. *J Synchrotron Radiat*, 23:1474–1483, 2016.

[30] A. Morawiec. *Orientations and Rotations*. Springer, 2004.

[31] L. Renversade, R. Quey, W. Ludwig, D. Menasche, S. Madalli, R.M. Suter, and A. Borbély. Comparison between diffraction contrast tomography and high energy diffraction microscopy on a slightly deformed aluminium alloy. *IUCrJ*, 3:32–42, 2016.

[32] T.H. Rowan. *Functional Stability Analysis of Numerical Algorithms*. PhD thesis, 1990.

[33] S.G. Johnson. The NLopt nonlinear-optimization package. *http://ab-initio.mit.edu/wiki/index.php/NLopt*.

[34] R. Quey, P.R. Dawson, and F. Barbe. Large-scale 3D random polycrystals for the finite element method: generation, meshing and remeshing. *Comput. Methods Appl. Mech. Eng.*, 200:1729–45, 2011.

[35] R. Quey and L. Renversade. Optimal polyhedral description of 3D polycrystals: method and application to statistical and synchotron X-ray diffraction data. *Comp. Methods Appl. Mech. Eng.*, 330:308–33, 2018.

[36] S.L. Wong and P.R. Dawson. Influence of directional strength-to-stiffness on the elastic-plastic transition of fcc polycrystals under uniaxial tensile loading. *Acta Mater.*, 58:1658–1678, 2010.

[37] Ch. Geuzaine and J.-F. Remacle. Gmsh: a three-dimensional finite element mesh generator with built-in pre- and post-processing facilities. *International Journal for Numerical Methods in Engineering*, 79:1309–1331, 2009.

[38] C. Lautensack and S. Zuyev. Random Laguerre tessellations. *Adv. Appl. Prob.*, 40:630–650, 2008.

[39] N. R. Barton and P. R. Dawson. On the spatial arrangement of lattice orientations in hot-rolled multiphase titanium. *Model. Simul. Mater. Sci. Eng.*, 9:433–463, 2001.

[40] F. Frank. Orientation mapping. *Metall. Mater. Trans. A*, 19:403–408, 1988.

[41] R. Quey. On the statistical significance of grain-scale lattice rotation resuts. *Mater. Charac.*, 193:112252, 2022.